On the role of energy dissipation in a dynamically structured fluidized bed

Victor Francia, Kaiqiao Wu and Marc-Olivier Coppens[1]

Department of Chemical Engineering and Centre for Nature Inspired Engineering, University College London, Torrington Place, London WC1E 7JE, United Kingdom.

Abstract

This work explores the effect of interparticle friction on the stability of a structured bubble flow in gas-solid fluidized beds. We provide a detailed quantification of the evolution of bubble properties at varying frequency, comparing experiments with CFD-DEM (computational fluid dynamics – discrete element modeling) simulations. Friction plays a key role. It creates intermittent solid-like regions that restrict the mobility of solids and endow the flow with enough memory to correlate consecutive nucleation events. As friction decreases, solid-like regions widen, allowing the circulation of solids; simultaneously, bubbles grow, move apart and ultimately break up the structure. CFD-DEM reproduces this phenomenon well in a small bed, but shows qualitative differences in bubble shape and acceleration. These deviations propagate into substantial errors at higher frequency or larger domains displaying multiple bubble rows, which stresses the need for further research to understand the effects of other particle properties, polydispersity and the domain size.

Keywords: fluidization; intensification; friction; bubbling; oscillatory flow; CFD-DEM

1. Introduction

Gas-solid suspensions are fundamentally unstable. They feature complex flow structures that are neither scalable nor easy to predict. For that reason, the design and operation of gas-solid fluidized beds is highly empirical, despite their extensive industrial use (Rüdisüli et al., 2012). Advanced design concepts aim to create "structured" beds, in which the gas-solid flow is made more predictable, typically more homogenous or controllable (Francia et al., 2021). To do so, one must find additional degrees of freedom to stabilize the flow. For example, one can manipulate the fluidization behavior with internals or injectors to redirect the gas, use a vortex flow or rotational boundaries to impart angular momentum, or apply external electrical or magnetic fields. It is possible to use additional energy sources, such as electromagnetic radiation, pressure waves or vibration to improve the gas-solid contact or to create a coherent flow structure (Francia et al., 2021). Vibration in particular has been widely applied in dryers as a way to enhance the flowability of cohesive mixtures (Jia et al., 2016, 2017; Jia et al., 2015). One obtains a similar effect using an oscillating inlet gas flow, which is often easier and less capital intensive (Akhavan et al., 2008; Ireland et al., 2016). Either through vibration or pulsation, a periodic excitation is known to homogenize a fluidized bed and improve interfacial contact. The agitation breaks local particle clusters that would otherwise interfere with the motion of the solids, but, unfortunately, this phenomenon is specific to the feedstock, operating conditions and the scale of the unit. A more robust design approach targets the formation of a scalable flow. This can be achieved by taking advantage of the self-assembly behavior of granular matter.

Powders have complex rheology that bear only some similarities with simple fluids or solids, but also nonlinear behavior not seen in either one (Aranson and Tsimring, 2009; Jaeger and Nagel, 1992; Jaeger et al., 1996; Kunii and Levenspiel, 2013). When exceeding a critical packing limit, they stay in a dense, quasi-static regime, in which particles interact via sustained friction. However, when strongly agitated (e.g., by vibration or fluidization),

1 - corresponding author

particles flow rapidly and collectively behave as a fluid, and phase separation may occur (Pak and Behringer, 1994). The balance between the energy input and the highly nonlinear dissipation due to particle collisions gives rise to macroscopic phenomena, such as clustering, which are difficult to predict from individual interactions. One prime example of these mesoscopic structures (Campbell, 1990; van den Bleek et al., 2002) is the ability of granular media to organize into near-perfectly ordered surface waves in vibrated (Clément and Labous, 2001) or pulsed (Figure 1a) shallow granular layers (de Martín et al., 2018). These structures are lost in a larger pulsed bed, because they are overcome by hydrodynamic instabilities, leading to bubbling or channeling (Jia et al., 2017). However, under the right conditions, the multiphase dynamics can synergistically interact through an external excitation, which contains the bubbling instability and makes the flow scalable and predictable (Francia et al., 2021).

1.1. Pattern Formation in Granular Systems Under Periodic Excitation

When vibrated periodically *in vacuo*, a thin granular layer of a few particle diameters deep organizes into a variety of surface patterns consisting of a grid of alternating squares or stripes (Clément et al., 1996; Douady et al., 1989; Melo et al., 1994, 1995), reminiscent of Faraday waves in vibrated liquid layers (Faraday, 1831). Excellent progress has been made in the study of surface waves in vertically shaken granular layers (Bizon et al., 1998; Carrillo et al., 2008). Computational models provide insight into the underlying physics (Bougie and Duckert, 2011; Bougie et al., 2002; Clément and Labous, 2001) and are the basis for phenomenological approaches describing them as harmonic oscillators (Tsimring and Aranson, 1997). A similar phenomenon appears when a layer is excited by a periodic fluid-particle force (Coppens et al., 2002; Coppens and van Ommen, 2003), see Figure 1a, but the origin and stability of these structures are far less understood. The work of de Martín et al. (de Martín et al., 2018) shows similarities to mechanically vibrated layers *in vacuo* and establishes a universal stability curve for gas-driven surface waves derived exclusively from hydrodynamic criteria, and including the terminal velocity of the particles. Comparable to a Faraday instability, the pattern wavelength in shallow oscillating layers is also proportional to f^{-2}.

The patterns formed under vibration are more difficult to be sustained in larger beds, because part of the energy input from the top or bottom plates dissipates through inelastic particle contacts, as the stress is transmitted into the bed. In a gas-driven system, patterns could survive further, because the gas fills interparticle voids and imposes a drag force directly and simultaneously onto every particle in the bed. However, increasing the height to a few tens of particle diameters introduces a primary hydrodynamic instability. In Geldart B suspensions (i.e., sand-like particles), the bubbling instability normally overcomes the surface wave formed by the gas oscillation, and the system degenerates into chaotic dynamics comparable to those under a constant gas flow. However, specific oscillating conditions can contain this process and make bubbles self-organize in a predictable manner. Figure 1b illustrates the macroscopically structured state, and Figure 1c shows the details of the bubble nucleation within two consecutive pulses. A gas channel forms when the air velocity increases and then breaks into bubbles aligned horizontally. The rupture of the channel is dictated by the position of the bubbles formed in the previous pulse, and the nucleation sites alternate in every other pulse, which arranges the bubbles in a triangular lattice of a characteristic wavelength, defined by a horizontal distance λ, and a polar angle θ, see Figure 1b. This phenomenon is not a simple resonance effect, and it does not share exactly the underlying physics observed in vibrated granular

systems. The self-organization is found to be independent of the bed width (Coppens et al., 2002), and so it must stem from a local force balance.

1.2. Propagation of a Granular Pattern into a Structured Flow

Few authors have studied computationally the formation of a structured bubble flow in pulsed fluidized beds. After 1D studies around the start of this century (van de Klundert, 2001), the work of Kawaguchi et al. (Kawaguchi et al., 2001) looked at the creation of coherent flow structures under pulsation. They concluded that pulses between 4 Hz and 5 Hz homogenize the bubble flow in Geldart B powders, but they could not replicate the self-organization observed experimentally. Two large bubbles formed and aligned horizontally, but always at the same positions, forming a square instead of a triangular lattice. Later works by Wang and Rhodes (Wang and Rhodes, 2005) reported similar conclusions within a range of frequencies between 5 and 10 Hz. In both cases, bubble nucleation was initiated from a horizontal channel spanning the bottom of the bed, but, in the simulations, the breakage into bubbles was neither reproducible nor in the correct positions. These earlier works concluded that pulsation homogenized a bed and somehow improved the "regularity" of the bubble flow, but only recently has the actual bubble pattern been convincingly replicated (Wu et al., 2017). In this work, the formation of a pattern was related to the creation of compressive stresses in the wake of rising bubbles. It is worth noticing that bubble self-organization is not the only possible recursive flow structure under pulsation. Researchers at the National Energy Technology Laboratory (NETL) and MIT have studied the formation of recursive bubbling flows in a small quasi-2D pulsed fluidized bed, 5 cm × 0.5 cm (Bakshi et al., 2018a; Bakshi et al., 2018b), pulsed between 5 Hz and 6 Hz for Geldart B particles. The bed was operated under much lower superficial gas velocities, where self-organization would not occur in a wider bed, and so the reproducible flow structure that appears is likely the result of the influence of the lateral walls in the solid circulation. Thus, not only the control of local bubble interactions, but device-specific boundary effects could be used to structure small beds. Computational work in the same system studied the effects of multiple parameters in a discrete modeling framework (Bakshi et al., 2018b), concluding that the creation of a coherent structure depends on the level of energy dissipation.

Every effort to date in the study of bubble patterns using Eulerian-Eulerian or two-fluid models (TFM) has proven unable to reproduce the experimentally observed self-organization. A classic implementation of a TFM was

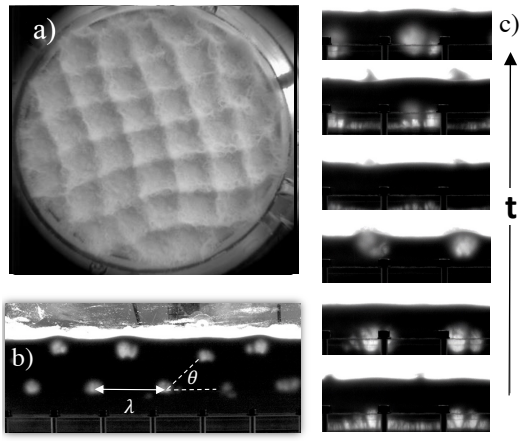

Figure 1 *– Pattern formation in fluidized beds when using an oscillating air flow. The particles are glass beads with d_p = 238 μm. The air velocity $u = u_{\min} + u_a\,[1 + \sin(2\pi\, f\, t)]$. a) Cylindrical 3D bed (14 cm diameter × 3 mm deep); $u = 1.5 + 0.8\,[1 + \sin(2\pi\, 17\, t)]$, b) Quasi-2D bed (45 cm × 1 cm × 10 cm); $u = 0.5 + 2.14\,[1 + \sin(2\pi\, 5\, t)]$, c) Quasi-2D bed (45 cm × 1 cm × 5 cm); $u = 0.5 + 2.14\,[1 + \sin(2\pi\, 5\, t)]$ showing snapshots taken over ~0.22 s.*

shown to reproduce the main bubbling statistics in large pulsed systems but not the bubble lattice (Wu et al., 2016). Later, Bakshi et al. reported computational work comparing 2D and 3D simulation domains with a continuum model (Bakshi et al., 2018a). They observed differences in bubbling behavior due to wall friction. 3D simulations seemed to provide a more reproducible (yet unstable) set of nucleation sites, but the arrangement obtained did not represent the triangular lattice observed experimentally. More recently, Ding et al. demonstrated that a 2D TFM, coupling a tuned frictional stress model, could reproduce some eposides of bubble alternation, although the structures formed often collapsed and could not be sustained over time (Ding et al., 2021). It is noteworthy that self-organization in deep beds is only observed experimentally when the bed operates under very dense conditions and oscillates across the minimum fluidization conditions, where the flow transitions between inertial and quasi-static regimes. This explains the lack of accuracy of TFM models and reflects an important issue in the utilization of continuum models for studying bubbling beds.

To address this question and shed some light onto the origin and stability of bubble self-organization, this work studies the behavior of a structured quasi-2D pulsed fluidized bed at different frequencies and compares the experimental behavior with computational work using Eulerian-Lagrangian or CFD-DEM (computational fluid dynamics – discrete element modeling) and TFM approaches. We investigate the role that friction plays in the emergence and stability of a structured flow, looking at the bubble nucleation, rise and rupture cycles by varying the interparticle friction coefficient, and examining the differences between TFM and CFD-DEM simulations. The dissipation of energy through friction appears to be fundamental. When it is sufficiently large, it impedes the lateral movement of the solids between the bubble wakes. In doing so, it restricts the circulation of solids to the areas between the bubbles, which in turn correlates their nucleation in consecutive pulses. Otherwise, the mobility of the solids is overpredicted, allowing for long-range circulation, excessive bubble growth, and, ultimately, chaotic behavior.

2. Experimental Setup

Experiments are conducted in a rectangular, pseudo-2D cell, 45 × 1 × 120 cm, made of transparent Perspex. The bed is connected to a plenum chamber and an air delivery system. Ambient air is filtered to remove dust and moisture, and pumped through a 5 L reservoir at 3 bar to mitigate any backflow effect caused by the pulsation. The airflow is then diverted into two parallel lines, equipped with either a needle or a solenoid valve (200 SLPM) and followed by OMEGA flow meters (250 SLPM). The air is first delivered to a plenum chamber in Perspex (45 × 1 × 20 cm), packed with corkscrew shaped filling (12 mm x 40 mm) that helps to distribute the flow homogeneously to a sintered metal distributor plate, which separates the plenum from the bed chamber.

During operation, the needle valve is kept at a set position, and the oscillating air flow with amplitude u_a and frequency *f* is generated by manipulating the solenoid valve (in-house LabVIEW). To ensure an accurate reading of u_a at the entrance of the bed, the measurement of the flow rate is correlated to instantaneous pressure measurements across the distributor using GE differential pressure sensors flush with the wall, Figure 2. The pressure sensors are calibrated to the readings of the OMEGA flow meters, using a set of constant flow rates spread within the working range. This calibration is later used to compute the instantaneous flow rate during the pulsed operation using differential pressure measurements at a sampling frequency of 1000 Hz. Different types

of distributors were tested within relevant flow ranges. A 3 mm grade 07 Sintertech Poral bronze plate, was found to be the most adequate to achieve sufficient pressure drop to avoid damping the amplitude, while distributing the flow evenly. Table 1 summarizes the operating conditions in experiments and simulations. Experiments are conducted using Jencons-PLS spherical soda-lime glass beads with a static bed height of 4.5 cm.

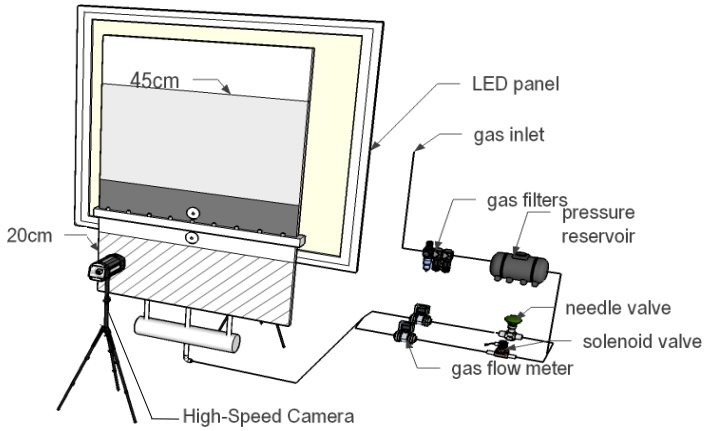

Figure 2 – *Experimental setup with a quasi-2D fluidized bed, making use of needle and solenoid valves to generate an oscillating air flow.*

Table 1. *Geometry and operating conditions.*

Geometry		
Width	4.5×10^{-1}	m
Height	1.2	m
Thickness	1.0×10^{-2}	m
Solid phase		
Particle loading, H_o	4.5×10^{-2}	m
Minimum fluidization velocity, u_{mf}	4.6×10^{-2}	$m\cdot s^{-1}$
Particle density, ρ_s	2500	$kg\cdot m^{-3}$
Particle diameter, d_s	224-250	μm
Angle of repose, θ_f	20.6	°
Gas phase		
Normalized pulse offset, $\hat{u}_{min}$	0.45	-
Normalized pulse amplitude, $\hat{u}_a$	1.90	
Pulse frequency, f	5, 7	s^{-1}
Gas density, ρ_g	1.225	$kg\cdot m^{-3}$
Gas viscosity,μ_g	1.8×10^{-5}	$kg\cdot m^{-1}\cdot s^{-1}$

The measured minimum fluidization velocity is u_{mf} = 0.046 m/s. Experiments and simulations are conducted by setting an oscillating superficial air velocity u, according to:

$$u = u_{\min} + u_a\,[1 + \sin(2\pi\, f\, t)] \qquad (1)$$

where f is the frequency of the applied oscillation, u_{min} is the minimum superficial gas velocity and u_a is the amplitude of the pulse. The resulting time-averaged velocity is $\bar{u} = u_{min} + \hat{u}_a$. Eq. (1) is rewritten in terms of dimensionless velocities, after division by the experimental minimum fluidization velocity u_{mf} , $\hat{u} = u/u_{\mathrm{mf}}$

$$\hat{u} = \hat{u}_{min} + \hat{u}_a\,[1 + \sin(2\pi\, f\, t)] \qquad (2)$$

3. Continuum and Discrete Theoretical Frameworks

Two computational platforms are employed, a Eulerian-Eulerian approach, known as the two-fluid model (TFM), and a Eulerian-Lagrangian approach (CFD-DEM). The commercial software Ansys Fluent 12 was used to conduct

TFM simulations; the CFD-DEM simulations were implemented in open-source code CFDEM, version 11, 3.1.0, which employs a four-way coupled method (Goniva et al., 2012).

3.1. Continuity and momentum transport

The TFM formulation depicts the gas and the solids as interpenetrating continua, coupled through a momentum exchange term. Both are described by continuity and momentum equations, Table 2 (van Wachem et al., 2001), with a Newtonian strain rate-stress relation for the gas stress tensor. The gas is treated as isothermal and incompressible, given the low Mach numbers involved. The key difference with classical fluid mechanics is the transport of momentum in the solid phase. A Eulerian model formulates a momentum transport equation that requires a set of closures for the solid stress term and its transport properties, solid bulk and shear viscosities (van Wachem et al., 2001). In this work, we use the solid pressure and bulk viscosity models of Lun et al. (Lun et al., 1984) (Table 2). The effective solid viscosity is associated with the way in which the particle movement transports momentum. In a dilute system, it includes collisional and kinetic contributions, whereby collisional transport accounts for momentum exchanged in instantaneous particle collisions and kinetic transport features the momentum transferred by convection. A set of constitutive expressions links the effective solid viscosity to the energy contained in particle fluctuations, quantified by a so-called granular temperature Θ. The granular temperature Θ satisfies a separate transport equation for the pseudo-thermal energy. As the granular matter flows, expands and contracts, the changes in Θ are described in an analogous way to the kinetic theory of molecular gases, through the kinetic theory of granular flow, KTGF. This assumes a dilute system, in which interparticle contacts are instantaneous, frictionless and binary, solid velocities are uncorrelated, and the spatial contact distribution is isotropic. A standard formulation (Hernández-Jiménez et al., 2011) is employed here, utilizing the diffusion of thermal energy proposed by Gidaspow (Gidaspow, 1994). In contrast, a Lagrangian model (DEM) requires no prior assumption on the distribution of the solids and explicitly solves the particle-particle momentum transport using a particle contact model. The CFD-DEM simulations follow the trajectories of all individual particles of size d_s and density ρ_s. For each particle, the translational velocity $\mathbf{U_s}$ and rotational velocity $\boldsymbol{\omega}_s$ are computed according to Newton's laws of motion, Eq.20 and Eq.21 in Table 2. Each particle-particle contact process is discretized in time, applying a Hertzian spring-dashpot model, Eq.22 and Eq.23.

3.2. Frictional stress correlation

Both continuous and discrete models predict accurately the stress and Θ in frictionless granular flow at low solid fractions. As the powder becomes more concentrated, however, interparticle collisions multiply and multi-particle contacts become more frequent. The flow transitions to an inertial and, ultimately, a quasi-static regime where the powder does not flow but deforms under shear. This process is conditioned by the microstructure of the force chains created when particles cluster. It is poorly understood, but it is accepted that beyond a critical void fraction, or jamming point, the transmission of stress through sustained contacts, e.g., particle chains, becomes dominant (Chialvo and Sundaresan, 2013). For that reason, the KTGF vastly underestimates the loss of kinetic energy due to clustering, consolidation and friction in dense flows. A standard TFM handles this by modifying the classic formulation with corrections aimed at introducing friction as a third way to transport momentum. A predefined frictional packing limit, ϕ_f, is set (typically independent of the particle type) above which a compensation term applies to the solid pressure. Frictional stress models borrowed from soil mechanics are used to compute a

frictional term in the solid stress using the isotropic pressure. In this work, we employ the methods of Shaeffer (Schaeffer, 1987) and Syamlal et al. (Syamlal et al., 1993), which have been widely adopted in modeling fluidized beds. More advanced TFM formulations include the transport of rotational granular energy to account for frictional dissipation in the inertial regime (Yang et al., 2016a; Yang et al., 2016b), the use of advanced local correlations between strain rate and stress to handle the dilute-to-dense transition (Jop et al., 2006; Pouliquen and Forterre, 2002), modifications to classic KTGF to include frictional energy dissipation and force chain effects, and non-local laws to address quasi-static flow behavior (Kamrin and Koval, 2012). These are promising steps to describe dynamic viscoplastic granular flow (Wu et al., 2020), but are not generally available in the fluidization community yet.

In a Lagrangian framework, the resolution of frictional contacts and multi-particle contacts is simpler. In CFD-DEM we employ a soft-sphere contact method to track the entire collision process for every particle contact pair. In this way, the model is suited to track inhomogeneous regions and anisotropic transport of momentum. The effects of friction are naturally accounted for by the spring-dashpot contact model and the application of Coulomb's law in each collision (Eq.24 in Table 2), along with the solution of the angular momentum balance.

3.3. Interphase momentum exchange

The particle-fluid interaction force is accounted for in an exchange term in the momentum equation for the solid phase, Eq. 5. Lift or virtual mass forces are found to be negligible, so that only drag and buoyancy forces are considered (Jackson, 2000). We employ the Gidaspow drag correlation (Gidaspow et al., 1991) in both the TFM and the CFD-DEM frameworks. In the CFD-DEM model, the fluid-particle interaction force $\mathbf{F}_f$ exerted on each spherical particle is given by Eq. 25, comprising of a pressure gradient term, accounting for buoyancy, and a drag force that is given by the relative velocity between gas and solids, multiplied by a drag coefficient per unit volume β. The momentum exchange term $\mathbf{M}_s$ in the Eulerian grid of the CFD-DEM method is mapped by the summation of the drag force term contained in $\mathbf{F}_f$ over all the particles in a cell, using an interpolation factor ζ_i to weigh their contribution based on their relative position to the centroid of the cell.

3.4. Boundary conditions, parameters and numerical settings

Zero-flux boundary conditions are assigned to the front and rear walls. Particle-wall contacts in CFD-DEM follow the same restitution and friction coefficient as the interparticle contacts, while partial slip walls are employed in the TFM to replicate the wider 2D experimental setup in a thinner computational domain. The generation of a structured flow relies on strong interphase coupling. Careful selection of the mesh size and time step is required. We employ a structured mesh, consisting of a single layer of cubic cells of 2 mm edge size, which ensures that the computed static solid packing is physical and grid-independent. According to Kuipers and colleagues, an increase in the number of cells in the third direction in such a narrow system has no significant effect on the overall dynamics (Goniva et al., 2012; Yang et al., 2016b). The solid phase time step is refined against Van der Hoef et al.'s criterion to 1×10^{-6} s (Silbert et al., 2001; van der Hoef et al., 2006), while a time step of 1×10^{-4} s is employed to fulfil the Courant–Friedrichs–Lewy condition (CFL) (Courant et al., 1967). Materials of well-known mechanical properties are used to ensure that the parameters used in the particle contact models and constitutive relations are accurate. Table 3 summarizes the values employed for Jencons-PLS spherical soda-lime, based on literature and an in-house sensitivity study on the effect that a realistic range has on the pattern formation. The interparticle friction coefficient, μ_f, is set according to the measurement of the angle of repose and it is reduced in

Table 2. *Mass and momentum conservation. Sub-models in TFM and CFD-DEM.*

TFM and CFD-DEM: Mass and momentum conservation for gas

$$\frac{\partial(\varepsilon\rho_{\mathrm{g}})}{\partial t}+\nabla\cdot\left(\varepsilon\rho_{\mathrm{g}}\mathbf{U}_{\mathrm{g}}\right)=0 \quad (3)$$

$$\frac{\partial(\varepsilon\rho_{\mathrm{g}}\mathbf{U}_{\mathrm{g}})}{\partial t}+\nabla\cdot(\varepsilon\rho_{\mathrm{g}}\mathbf{U}_{\mathrm{g}}\mathbf{U}_{\mathrm{g}})=-\varepsilon\nabla P+\nabla\cdot\bar{\bar{\tau}}_{\mathrm{g}}+\varepsilon\rho_{\mathrm{g}}\mathbf{g}-\beta(\mathbf{U}_{\mathrm{g}}-\mathbf{U}_{\mathrm{s}}) \quad (4)$$

TFM: Closures and governing equations for solids

$$\frac{\partial(\phi\rho_{\mathrm{s}}\mathbf{U}_{\mathrm{s}})}{\partial t}+\nabla\cdot(\phi\rho_{\mathrm{s}}\mathbf{U}_{\mathrm{s}}\mathbf{U}_{\mathrm{s}})=-\phi\nabla P-\nabla P_{\mathrm{s}}+\nabla\cdot\bar{\bar{\tau}}_{\mathrm{s}}+\phi\rho_{\mathrm{s}}\mathbf{g}+\beta(\mathbf{U}_{\mathrm{g}}-\mathbf{U}_{\mathrm{s}}) \quad (5)$$

$$\frac{3}{2}\left[\frac{\partial(\phi\rho_{\mathrm{s}}\Theta)}{\partial t}+\nabla\cdot(\phi\rho_{\mathrm{s}}\mathbf{U}_{\mathrm{s}}\Theta)\right]=(-P_{\mathrm{s}}\bar{\bar{I}}+\bar{\bar{\tau}}_{\mathrm{s}}):\nabla\mathbf{U}_{\mathrm{s}}-\nabla\cdot(\kappa\nabla\Theta)-\gamma-3\beta\Theta \quad (6)$$

Bulk viscosity, λ_{s} (Lun et al., 1984)

$$\lambda_{\mathrm{s}}=\frac{4}{3}\phi\rho_{\mathrm{s}}d_{\mathrm{s}}g_{0,\mathrm{ss}}(1+e)\left(\frac{\Theta}{\pi}\right)^{1/2} \quad (7)$$

Radial distribution function, $g_{0,\mathrm{ss}}$ (Lun et al., 1984)

$$g_{0,\mathrm{ss}}=\left[1-\left({}^{\phi}/_{\phi_{\max}}\right)^{1/3}\right]^{-1} \quad (8)$$

Solid pressure (KTGF contribution), $P_{\mathrm{s}}^{\mathrm{v}}$ (Lun et al., 1984)

$$P_{\mathrm{s}}^{\mathrm{v}}=\phi\rho_{\mathrm{s}}\Theta+2\rho_{\mathrm{s}}(1+e)\phi^2g_{0,\mathrm{ss}}\Theta \quad (9)$$

Collisional viscosity, $\mu_{\mathrm{s}}^{\mathrm{col}}$ (Gidaspow, 1994)

$$\mu_{\mathrm{s}}^{\mathrm{col}}=\frac{4}{5}\phi\rho_{\mathrm{s}}d_{\mathrm{s}}g_{0,\mathrm{ss}}(1+e)\left(\frac{\Theta}{\pi}\right)^{1/2} \quad (10)$$

Kinetic viscosity, $\mu_{\mathrm{s}}^{\mathrm{kin}}$ (Gidaspow, 1994)

$$\mu_{\mathrm{s}}^{\mathrm{kin}}=\frac{10\rho_{\mathrm{s}}d_{\mathrm{s}}\sqrt{\Theta\pi}}{96\phi(1+e)g_{0,\mathrm{ss}}}\left[1+\frac{4}{5}g_{0,\mathrm{ss}}\phi(1+e)\right]^2 \quad (11)$$

Granular temperature modulus, κ (Gidaspow, 1994)

$$\kappa=\frac{150\rho_{\mathrm{s}}d_{\mathrm{s}}\sqrt{\Theta\pi}}{384(1+e)g_{0,\mathrm{ss}}}\left[1+\frac{6}{5}\phi g_{0,\mathrm{ss}}(1+e)\right]^2+2\rho_{\mathrm{s}}\phi^2d_{\mathrm{s}}(1+e)g_{0,\mathrm{ss}}\left(\frac{\Theta}{\pi}\right)^{1/2} \quad (12)$$

Collision dissipation, γ (Lun et al., 1984)

$$\gamma=\frac{12(1-e^2)g_{0,\mathrm{ss}}}{d_{\mathrm{s}}\sqrt{\pi}}\rho_{\mathrm{s}}\phi^2\Theta^{3/2} \quad (13)$$

Interphase drag coefficient, β (Gidaspow et al., 1991)

$$\beta=\tfrac{3}{4}C_{\mathrm{d}}\frac{\rho_{\mathrm{g}}\|\mathbf{U}_{\mathrm{g}}-\mathbf{U}_{\mathrm{s}}\|\varepsilon(1-\varepsilon)}{d_{\mathrm{s}}}\varepsilon^{-2.65} \quad \text{when } \varepsilon>0.8 \quad (14)$$

$$C_{\mathrm{d}}=\frac{24}{\varepsilon\mathrm{Re}}[1+0.15(\varepsilon\mathrm{Re})^{0.687}] \quad (15)$$

$$\mathrm{Re}\equiv\frac{\rho_{\mathrm{g}}}{\mu_{\mathrm{g}}}\left\|\mathbf{U}_{\mathrm{g}}-\mathbf{U}_{\mathrm{s}}\right\|d_{\mathrm{s}} \quad (16)$$

$$\beta=150\frac{(1-\varepsilon)^2\mu_{\mathrm{g}}}{\varepsilon d_{\mathrm{s}}^2}+1.75\frac{\rho_{\mathrm{g}}(1-\varepsilon)\|\mathbf{U}_{\mathrm{g}}-\mathbf{U}_{\mathrm{s}}\|}{d_{\mathrm{s}}} \quad \text{when } \varepsilon\leq0.8 \quad (17)$$

Frictional viscosity, $\mu_{\mathrm{s}}^{\mathrm{f}}$ (Schaeffer, 1987)

$$\mu_{\mathrm{s}}^{\mathrm{f}}=\frac{P_{\mathrm{s}}^{\mathrm{f}}\sin\theta_{\mathrm{f}}}{2\sqrt{\mathbf{S}_{\mathrm{s}}:\mathbf{S}_{\mathrm{s}}}} \quad (18)$$

Frictional pressure, $P_{\mathrm{s}}^{\mathrm{f}}$ (Syamlal et al., 1993)

$$P_{\mathrm{s}}^{\mathrm{f}}=A(\phi-\phi_{\mathrm{f}})^{\mathrm{n}} \quad (19)$$

DEM: Contact mechanics

$$m\frac{d\mathbf{U}_{\mathrm{s}}}{dt}=\boldsymbol{F}_{\mathrm{c}}+\boldsymbol{F}_{\mathrm{f}}+m\mathbf{g} \quad (20)$$

$$I\frac{\mathrm{d}\boldsymbol{\omega}_{\mathrm{s}}}{\mathrm{d}t}=\mathbf{T} \quad (21)$$

$$\mathbf{F}_{\mathrm{n}}=k_{\mathrm{n}}\boldsymbol{\delta}_{\mathrm{n}}-2\sqrt{\tfrac{5}{6}}\beta\sqrt{\tfrac{3}{2}k_{\mathrm{n}}m^*}\mathbf{U}_{\mathrm{n}} \quad (22)$$

$$\mathbf{F}_{\mathrm{t}}=k_{\mathrm{t}}\boldsymbol{\delta}_t-2\sqrt{\tfrac{5}{6}}\beta\sqrt{k_{\mathrm{t}}m^*}\mathbf{U}_t \quad (23)$$

$$\mathbf{F}_{\mathrm{t}}\leq\mu_{\mathrm{f}}\mathbf{F}_{\mathrm{n}} \quad (24)$$

$$\mathbf{F}_{\mathrm{f}}^i=-V_{\mathrm{i}}\nabla P-\frac{V_{\mathrm{i}}\beta_{\mathrm{d}}}{1-\varepsilon}(\mathbf{U}_{\mathrm{g}}-\mathbf{U}_{\mathrm{s,i}}) \quad (25)$$

$$\mathbf{M}_{\mathrm{s}}=\frac{1}{V_{\mathrm{c}}}\sum_{i=1}^{N}\frac{\zeta_{\mathrm{i}}V_{\mathrm{i}}\beta_{\mathrm{d}}}{1-\varepsilon}(\mathbf{U}_{\mathrm{g}}-\mathbf{U}_{\mathrm{s,i}}) \quad (26)$$

particle-wall collisions to avoid an unrealistic clogging effect in a narrow domain. The coefficient of restitution, e, and the Poisson ratio, υ, are set according to reported values (Foerster et al., 1994). We follow standard practice in coupled CFD-DEM simulations of slowly bubbling beds (Foerster et al., 1994; Müller et al., 2008) that incorporates an artificially small Young's modulus, E, to limit the time step required for the computation of particle contacts. For non-cohesive, Geldart B particles, it is generally accepted that changes above 800 N/s in the spring constant play no major role on the bubbling behavior (Mikami et al., 1998; Müller et al., 2008; Wang and Rhodes, 2005). Our numerical verifications demonstrate that the bubble size becomes independent of E above 10 MPa, and that it is independent of the restitution coefficient typically employed for glass beads.

3.5. Geometry independence

The triangular lattice formed by the bubbles in the dynamically structured regime is characterized by a horizontal pitch or wavelength λ, the polar angle θ between its elements and the bubble size D_b. It has been proven experimentally that, under the same conditions, a granular bed of the same static height develops a bubble pattern of the same λ, θ and D_b independently of the bed width (Coppens et al., 2002). In order to ensure that the CFD-DEM simulations are also independent of the domain width, domains 10 cm and 15 cm wide were considered. The results are indeed comparable, as illustrated in Figure 3. Subsequent computational work is conducted in the smaller domain to minimize the computational expense. The geometry is sufficiently large to display the simultaneous generation of two bubbles and the mechanism underpinning the generation of a periodic flow structure.

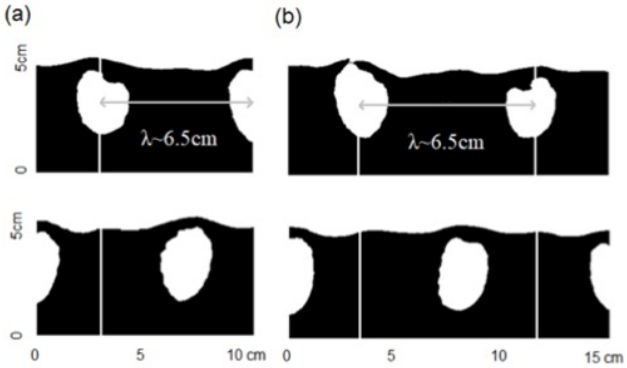

Figure 3 - *Width independence of CFD-DEM simulations of a dynamically structured fluidized bed, illustrated by snapshots of two consecutive pulses (top and bottom): (a) W = 10 cm (4.5cm × 0.2 cm × 10 cm) and (b) W = 15 cm (4.5cm × 0.2 cm × 15 cm), pulsated at* $\hat{u} = u/u_{mf} = 0.45 + 1.9\,[1 + \sin(2\pi\, 5\, t)]$.

4. Analysis

4.1. Bubble properties

The lattice parameters λ, θ and D_b are extracted from the analysis of experimental images or computational data, both sampled at 100 Hz, once a steady state is reached. The bubble population is identified using a threshold in the intensity of greyscale images or the computational void fraction (i.e., $\varepsilon > 0.8$ delimits the bubble phase). An equivalent spherical diameter is computed from the 2D bubble area, and the position is calculated as its center of mass. Velocity distributions are obtained with an in-house tracking algorithm. Voids smaller than 4 mm, irregularly shaped features close to the surface and channel-like voids, e.g., with a shape factor (longest divided by shortest chord length) above five, are excluded. Depending on the pulsating frequency, bubbles are staged in two rows (f = 7 Hz), or in one (f = 5 Hz). The wavelength λ of the pattern is defined as the median of the distances

***Table 3**. Settings for TFM and CFD-DEM simulations.*

	TFM	**CFD-DEM**
Geometry		
W (x direction)	1×10^{-1} m	
T (y direction)	2×10^{-3} m	
H (z direction)	4.5×10^{-2} m	
Grid mesh size d_c	2×10^{-3} m	
Walls - xz	No-slip for the gas phase	
Walls - yz	No-slip for the gas phase	
Inlet - xy	$\hat{u} = \hat{u}_{min} + \hat{u}_a[1 + \sin(2\pi f t)]$	
Outlet - xy	P = 101325 Pa	
Δt_g	10^{-4} s	10^{-4} s
Δt_s		10^{-6} s
Gas Phase		
ρ_g	1.225 kg·m^{-3}	
μ_g	1.8×10^{-5} Pa·s	
$\hat{u}_a$	1.90	
$\hat{u}_{min}$	0.45	
f	5 Hz or 7 Hz	
Solid Phase		
#	-	752385
H_o	4.5×10^{-2} m	4.5×10^{-2} m
u_{mf}	4.8×10^{-2} m·s^{-1}	5.5×10^{-2} m·s^{-1}
ρ_s	2500 kg m^{-3}	
d_s	238 μm	
E	-	10 MPa
e	0.97	0.97
υ	-	0.22
ϕ_f	Table 4	-
μ_f	-	Table 4
μ_w	-	0.10
θ_f	20.6	-

between centroids of neighboring bubbles, and a neighbor is defined as the closest bubble in a range of relative polar angle $-20^o < \theta < 20^o$.

A natural choice to study pulsating systems is the use of the phase angle of the perturbation φ, to describe many reproductions of the same point in a pulse. The phase angle is expressed as $\varphi = 2\pi\ (t/T\text{-}N)$, N being an integer and $T = 1/f$ the pulse period. The air reaches the same flow rate at a given φ for any pulse moving from a reference $N = i$ at $t = t_0$ to $N = i + j$ at $t = t_0 + jT$ for any i, j. This work studies the organization of bubbles into a subharmonic pattern, i.e., a pattern recurring at a lower frequency than the natural frequency. A triangular lattice, as in Figure 1b, arises when the bubble nucleation sites alternate, as in Figure 3. The same structure repeats itself every two periods, so that sampling the data at $f/2$ leads to two sets of possible nucleation sites, given by even pulse numbers $N = i$ (denoted set A) and odd pulse numbers $N = i + 1$ (denoted set B) separated as $\varphi_{i+1} = \varphi_i + 2\pi$. The reproducibility of the flow will be studied using the probability density map for the bubble phase. A 3D density function $f_b(x,y,\varphi)$ is computed to signal the probability of a point in space (x, y) to be contained in the bubble phase at any phase angle

φ. We define $f_b(x,y)$ as the time-averaged bubbling density function, and $f_{b,\varphi_0}(x,y)$ as the phase-averaged bubbling density function at φ_0; both are normalized over the (x, y) domain:

$$\iint f_b dxdy = 1 \tag{27}$$

$$\iint f_{b,\varphi_o} dxdy = 1 \text{ at } \varphi_o \tag{28}$$

While the spatial distribution of f_b during an entire period shows the most probable bubble trajectories, f_{b,φ_0} shows the most probable location of the bubble phase at a particular phase during each pulse. In a stochastic system, f_b and f_{b,φ_0} do not differ and correspond to a relatively uniform distribution (Figure 4b), reaching the same average value in every point, which is the overall concentration of the bubble phase. In contrast, in a perfectly periodic bubble flow, the bubble nucleation, growth or rupture occur at specific phase angles during the pulsation. Bubbles occupy the exact same space for a given set of phase angles (A or B) and f_{b,φ_0} shows a sharp boundary between the bubble and emulsion phase (Figure 4a).

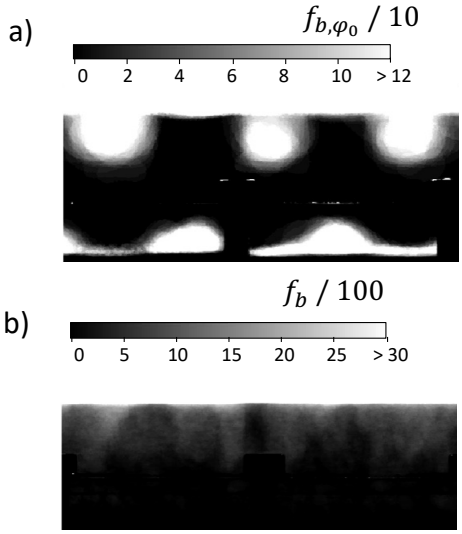

Figure 4 - *Bubble phase probability density map in a 10 cm × 10 cm domain for (a) oscillating flow for even pulses (set A, f_{b,φ_0} for $\varphi_o = 2\pi$) pulsated at $\hat{u} = u/u_{mf} = 0.45 + 1.9\,[1 + \sin(2\pi\, 7\, t)]$, and (b) f_b at constant flow with the same average gas flow rate, $\hat{u} = u/u_{mf} = 2.35$. Note the different scales in the grey bar.*

4.2. Solid pressure

CFD-DEM simulations provide a detailed force balance at the particle level. To obtain data directly comparable to the TFM formulation, the macroscopic solid stress tensor is reconstructed using the virial theorem (Chialvo et al., 2012) to map the particle contact forces onto the grid employed for the Eulerian simulations, using kinetic and collisional contributions:

$$\sigma_{s,ij} = \frac{1}{V_c}\sum_{k\in c}\left[\sum_{l\in c, l\neq k}\frac{1}{2}(x_i^{(k)} - x_i^{(l)})\, f_j^{(kl)} + m^{(k)}(v_i^{(k)} - \bar{v}_i)(v_j^{(k)} - \bar{v}_j)\right] \tag{29}$$

Here, $(x_i^{(k)} - x_i^{(l)})$ is the i direction component of the center-center contact vector from particle l to particle k , f_j is the contact force in the j direction, and $(v_i^{(k)} - \bar{v}_i)$ is the i direction fluctuating component of particle k to the bulk

streaming velocity. The ensemble-averaged pressure is computed from the isotropic terms and the macroscopic gradients are reconstructed using the same first-order central difference scheme used in the continuum simulations.

5. Results

Bubble self-organization occurs only in a bed where the flow periodically oscillates to flows below the minimum fluidization conditions. Previous work found that a discrete model can reproduce this phenomenon qualitatively with no fitting parameters (Wu et al., 2017). In this work, the self-organization is described in detail at different frequencies and computational simulations are used to study the role played by friction. On the one hand, frictional contacts are responsible for increasing energy dissipation and, on the other, they govern how and when the solid phase enters in a quasi-static regime. The following sections provide a quantitative comparison of experimental data with predictions of the CFD-DEM and TFM models under varying levels of interparticle friction (or critical void fraction) to assess how restrictions in solids mobility affect the self-organization. Table 4 summarizes the experiments and computational simulations. Experiments are conducted under the operating conditions in Table 1, at two different frequencies, 5 Hz (E5) and 7 Hz (E7). Both cases are modeled with a discrete formulation (CFD-DEM) under varying interparticle friction coefficient, μ_f, and, correspondingly, the continuum formulation (TFM) under the jamming or critical solid fraction in TFM, ϕ_f (Chialvo and Sundaresan, 2013). It should be noted that varying ϕ_f is clearly not equivalent to changing the interparticle friction coefficient, and can only serve as an approximation of its effects in a classic TFM implementation.

5.1. Structured Nucleation

A discrete model captures successfully the alternating bubble flows and provides a reasonable prediction of D_b and λ at different frequencies. The TFM formulation reproduces it neither qualitatively nor quantitatively (videos available as supplementary information).

Table 5 illustrates the fluidization conditions, including the expected bubble phase according to the two-phase theory (Toomey and Johnstone, 1952), whereby gas injected above minimum fluidization is used to create the bubble phase. The injection velocity oscillates with a mean above u_{mf} (i.e. $\bar{u} = u_{min} + u_a = 2.35$) but the bed operates below u_{mf} for a fixed period of time (22.3 % of the time during the phase angles $1.28\,\pi < \varphi < 1.72\,\pi$; note that this is independent of f and a function only of u_{min} and u_a). The integration of u during one pulsation cycle determines the expected bubble phase area A_{bt} in every row. A_{bt} drops by almost 30% from E5 to E7, due to the shorter duration of the pulse. In both cases, the maximum bubble phase area measured experimentally, $A_{b,max}$, is substantially lower.

Table 4. *Summary of Experiments and Simulations*

Experiments		**CFD - DEM**		**TFM**			
f / s^{-1}		f / s^{-1}		f / s^{-1}			
5	7	5	7	5	7	μ_f	ϕ_f (Chialvo et al., 2012)
		D5-0				0.0	
		D5-1		T5-1	T7-1	0.10	0.607
		D5-2				0.20	
		D5-3				0.30	
E5	E7	D5	D7	T5	T7	0.35	0.597
		D5-4				0.40	

Table 5. *Pulsed fluidization conditions.*

	A_{bt} / cm^2	$A_{b,max}$ / cm^2
E5	13.34	7.40 ($\varphi = 1.3\pi$)
D5	10.01	8.99 ($\varphi = 1.4\pi$)
T5	13.00	5.75 ($\varphi = 2.0\pi$)
E7	9.49	5.31 ($\varphi = 1.4\pi$)
D7	8.55	6.80 ($\varphi = 1.7\pi$)
T7	9.28	3.35 ($\varphi = 2.6\pi$)

* A_{bt} *: injected bubble area in every pulse from* t_0 *to* t_1, $A_{bt} = W \int_{t_0}^{t_1}(u(t) - u_{\mathrm{mf}})dt$.

** $A_{b,max}$ *: maximum area of bubbles in the same row (injected in the same pulse)*

The corresponding bubble size D_b is reduced by 36% when increasing the frequency from 5 to 7 Hz. This change in diameter is dictated by the way the bubbles self-organize into a periodic pattern. When bubbles arrange in a triangular lattice, the separation between neighbors is dictated by λ and θ, which leads to only two possible distances (one when $\theta_b = 60^o$). For E7, the vertical distance between consecutive horizontal rows reduces, due to the shorter duration of the pulse compared to E5; therefore, the bubbles are smaller and the horizontal wavelength λ must drop correspondingly to maintain the lattice. As a result, increasing f reduces both the overall bubble phase volume and the bubble separation (i.e., more smaller bubbles separated by shorter distances). The possible range of D_b and λ that can sustain a stable pattern must be related to the scale at which the circulation around a bubble can influence its immediate neighbors (6 in a triangular lattice); for that reason, D_b and λ are strongly correlated in dynamically structured beds. Both are seen to decrease for increasing frequencies until the lattice breaks down. This behavior has been observed experimentally over the quite wide investigated range of static heights (5 - 20 cm) and particle diameters (238 - 475μm) for the same material and specific combinations of f, u_{min} and u_a that exhibit regular bubble self-organization.

Figure 5 depicts the solid circulation using the time-averaged bubble phase density map, and Figure 6 describes the self-organization mechanism presenting the density maps for each phase angle. Bubbles are formed at specific sets of locations, and move axially along four preferential trajectories in E5 and D5, and five in E7 and D7, see Figure 5. The CFD-DEM framework predicts how the nucleation sites alternate, but it does not fully capture other qualitative features. As shown in Figure 5, in the experiments, a clear horizontal channel appears near the distributor, E5, and breaks at fixed positions. This process is repeated every other cycle with limited variability. During each cycle, bubbles rise with increasing lateral mobility, forming the inverted conical region shown in E5 and E7. In D5 and D7, however, no discernible horizontal channel appears. Instead, a larger area of high void fraction forms at the bottom as soon as the gas velocity u decreases at $\varphi = 0.5\pi$. This area grows until u drops below u_{mf} at ~1.28π and then it breaks into bubbles that change in shape while they are rising with negligible lateral mobility, which leads to the wider columns drifting outwards in Figure 6. This difference suggests that the presence of the walls in the computational domain plays a role, despite not affecting the overall bubble size and wavelength (Figure 3). TFM simulations, T5 and T7, show fundamentally different behavior. They render a stable recursive flow structure,

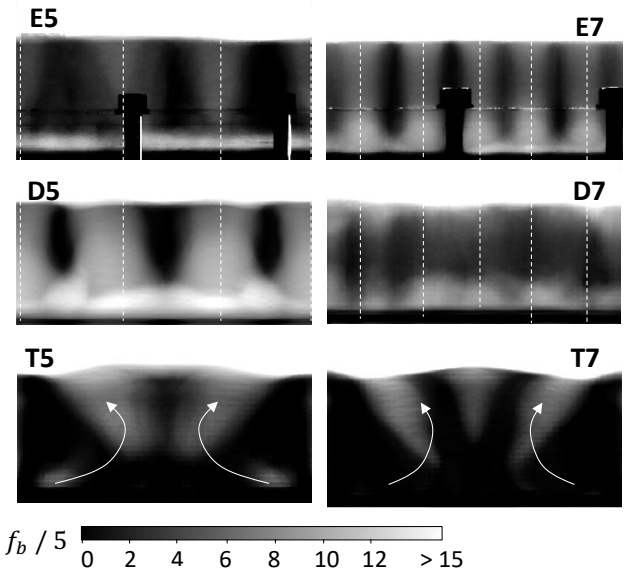

Figure 5 - *Bubble phase distribution. Bubble probability density maps f_b for the reference experiments (E5, E7), CFD-DEM (D5, D7) and TFM (T5, T7) simulations. Full conditions summarized in Tables 1, 3 and 4.*

albeit an incorrect one. During every pulse, smaller bubbles form at the bottom, flow inwards into an area of low void fraction in the center, grow and rise to the surface, forming 2 or 3 bubbles at 5 Hz or 7 Hz. The central flow pushes the powder aside at the top, which then flows back down near the walls, forming a long central recirculation loop. The flow structures in E5, E7, D5 and D7 alternate every pulse (recurring at 2/*f*), but the loop in T-5 and T-7 is repeated every pulse (recurring at 1/*f*).

Figure 6 illustrates the self-organization mechanism by dividing the pulsation into the nucleation, bubbling and rupture stages observed experimentally, and comparing them with computational predictions for a system with an array with a single (E5, D5, T5) or a double row (E7, D7, T7) of bubbles. Figures 7 to 10 provide the basis for quantifying the evolution of the bubble size, separation and velocity, and Table 6 summarizes the mean statistics during the bubbling stage.

Self-organization relies on the correlated motion of bubbles created in different pulses. In larger systems, bubbles survive in the bed during many pulsations, but, for a pattern to emerge, at least two pulses must be correlated.

Table 6. *Bubble properties: Experiments (E) vs CFD-DEM (D)*

Bubbling Phase		$D_{b,50}$	λ_{50}	$U_{b,50}$
		cm	cm	cm·s^{-1}
1.3 π – 2.1 π	E5	2.62	6.5	22.4
	D5	2.73	6.2	17.2
1.3 π – 2.6 π	E7	1.60	3.7	21.1
	D7	1.70	4.5	21.2

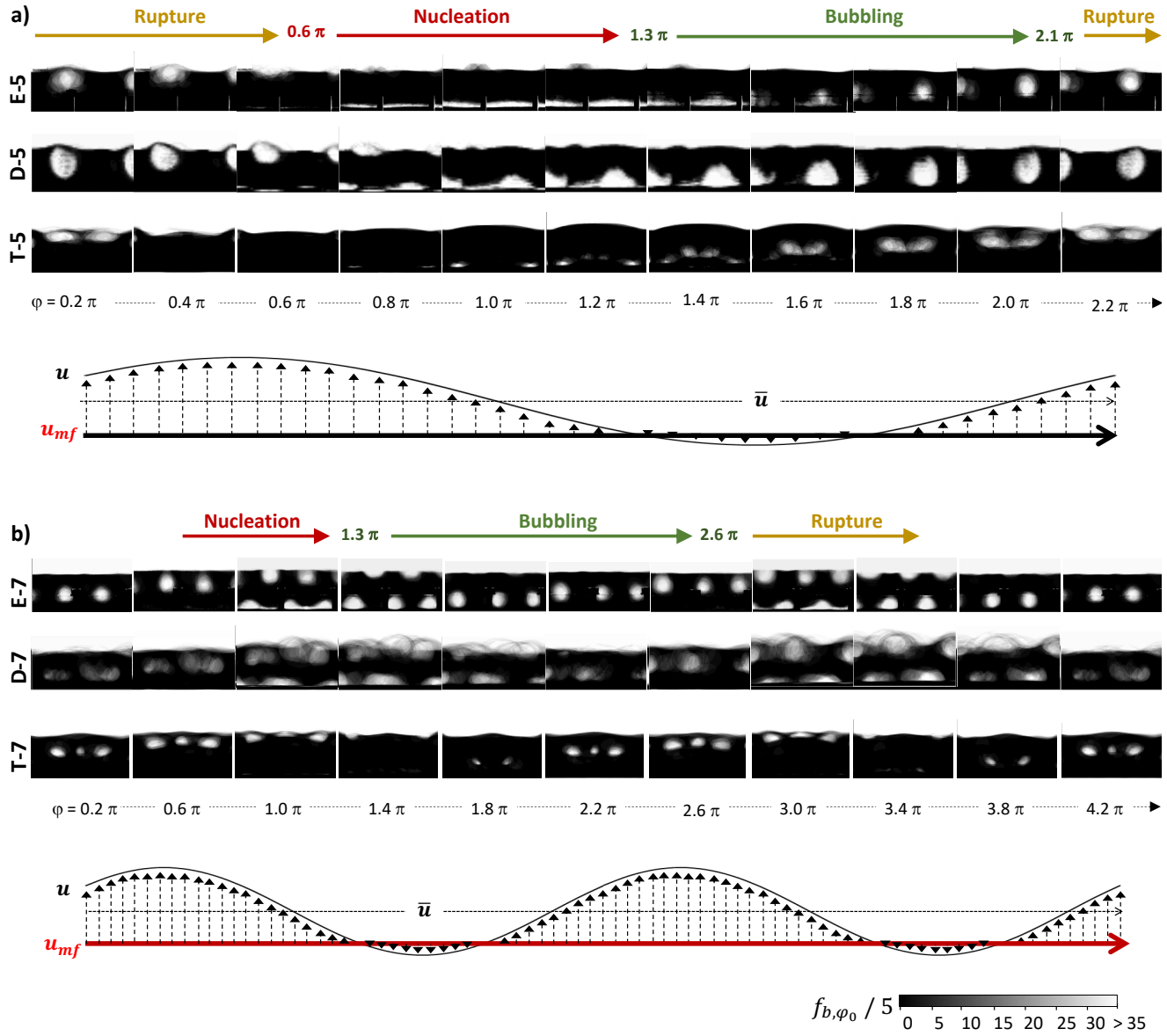

Figure 6. *Nucleation, bubbling and rupture cycles during the pulsation. Bubble phase probability density maps f_{b,φ_0} for even (E & D) or all pulses (T) for experiments (E), CFD-DEM (D) and TFM (T) simulations of bed with: a) a single-row array of bubbles (5Hz: E5, D5, T5); b) a double-row array of bubbles (7Hz: E7, D7, T7).*

In these experiments, bubbles formed during a pulse are still present in the bed during the next pulse (bubbles at the surface during the rupture stage in Figure 6) until $\varphi \sim 0.6\ \pi$ or $\varphi \sim 1.6\ \pi$ in E5 and E7. At the beginning of a new pulse, the gas velocity u increases from $\varphi = 0$ to $\varphi = \pi/2$, and the existing bubbles rise to the surface. In this period, when u exceeds u_{mf}, the gas lifts and accelerates the bed upwards. When u starts decreasing at $\varphi = \pi/2$, an incipient void forms at the bottom in both E5 and E7, and expands into a horizontal channel that keeps on growing. This is the start of the bubble nucleation stage. As the gas velocity u keeps dropping, the top of the bed decelerates and then starts to collapse, causing the channel to flow into the space left between the existing bubbles during $\varphi = 0.6 - 1.3\ \pi$. This stage is denoted the (bubble) nucleation stage, because the channel eventually breaks into two or three horizontally aligned bubbles when the gas velocity drops below u_{mf} at $\varphi \sim 1.3\pi$. The newly created structures contract and shape into new bubbles that rise to the surface, denoted bubbling stage. This stage extends for $1.3 - 2.1\ \pi$ in E5 and $1.3 - 2.6\ \pi$ in E7. The end of the bubbling stage is marked by the point where the bubbles decelerate reaching the surface, and eventually break during the rupture stage (see later Figure 7). This stage is

already part of the next pulsation at $2.1 - 2.6\,\pi$ (i.e., $0.1 - 0.6\,\pi$ for a consecutive pulse) in E5 and $2.5 - 3.5\,\pi$ (i.e., $0.6 - 1.5\,\pi$ for a consecutive pulse) in E7.

The discrete modelling framework is able to replicate this phenomenon qualitatively for both frequencies, D5 and D7, but it does not entirely capture the evolution of the bubble shape nor the stability of the lattice. D5 shows a stable pattern (Figure 6a), but simulations at a higher frequency D7 show far more variability and a shorter wavelength (Figure 6b). The nucleation also shows qualitative differences. Although bubbles are formed precisely at the same point, the discrete models do not predict a clear bottom channel, but a larger area of high void fraction that reshapes into a recognizable bubble sooner. In the TFM simulations, T5 and T7, the nucleation-bubbling-rupture cycle follows an entirely different dynamic. Critically, the bubbles formed in a previous cycle have already ruptured at $\varphi = 0$. When u starts decreasing for $\varphi > \pi/2$, there appears a central recirculation loop, where small bubbles are first formed at the sides of the bed, move inwards and coalesce to form a pair of central bubbles. This behavior translates in an increase in size and a drastic reduction of wavelength.

Figure 7 quantifies the experimental evolution of the bubble properties and Figure 8 illustrates the ability of computational models to track the size, the separation and velocity of the bubbles at 5 Hz and 7 Hz, corresponding to arrays of single and double rows of bubbles. In both cases, when the bed collapses at 1.3π, the bubbles form and

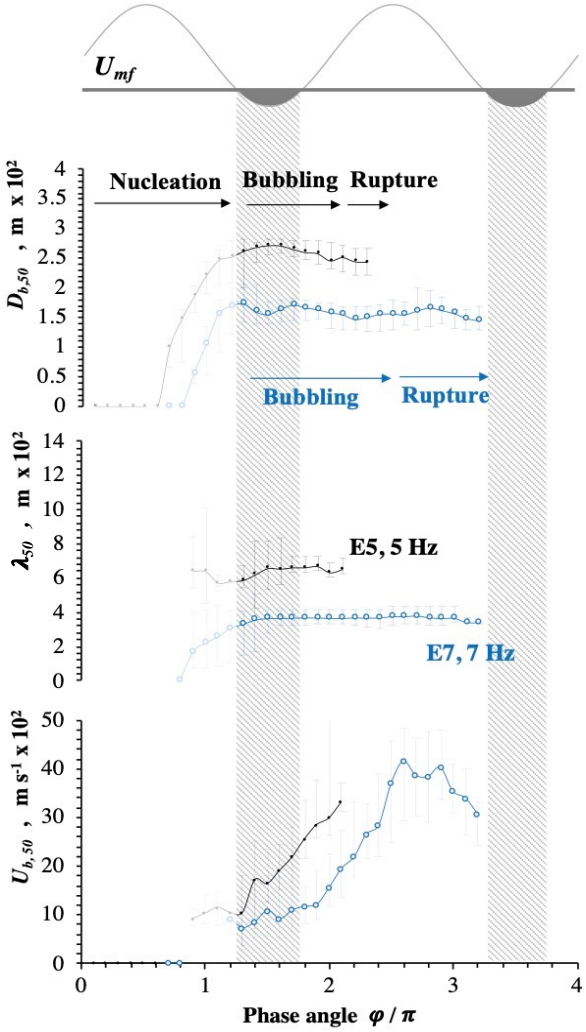

Figure 7 - *Bubble self-organization. Experimental evolution of the median bubble size $D_{b,50}$, wavelength λ_{50} and velocity $U_{b,50}$ in a structured bed formed of a single (E5, 5Hz) or a double-row (E7, 7Hz) array of bubbles. Markers denote the median p_{50}; error bars denote the range p_{10} to p_{90}.*

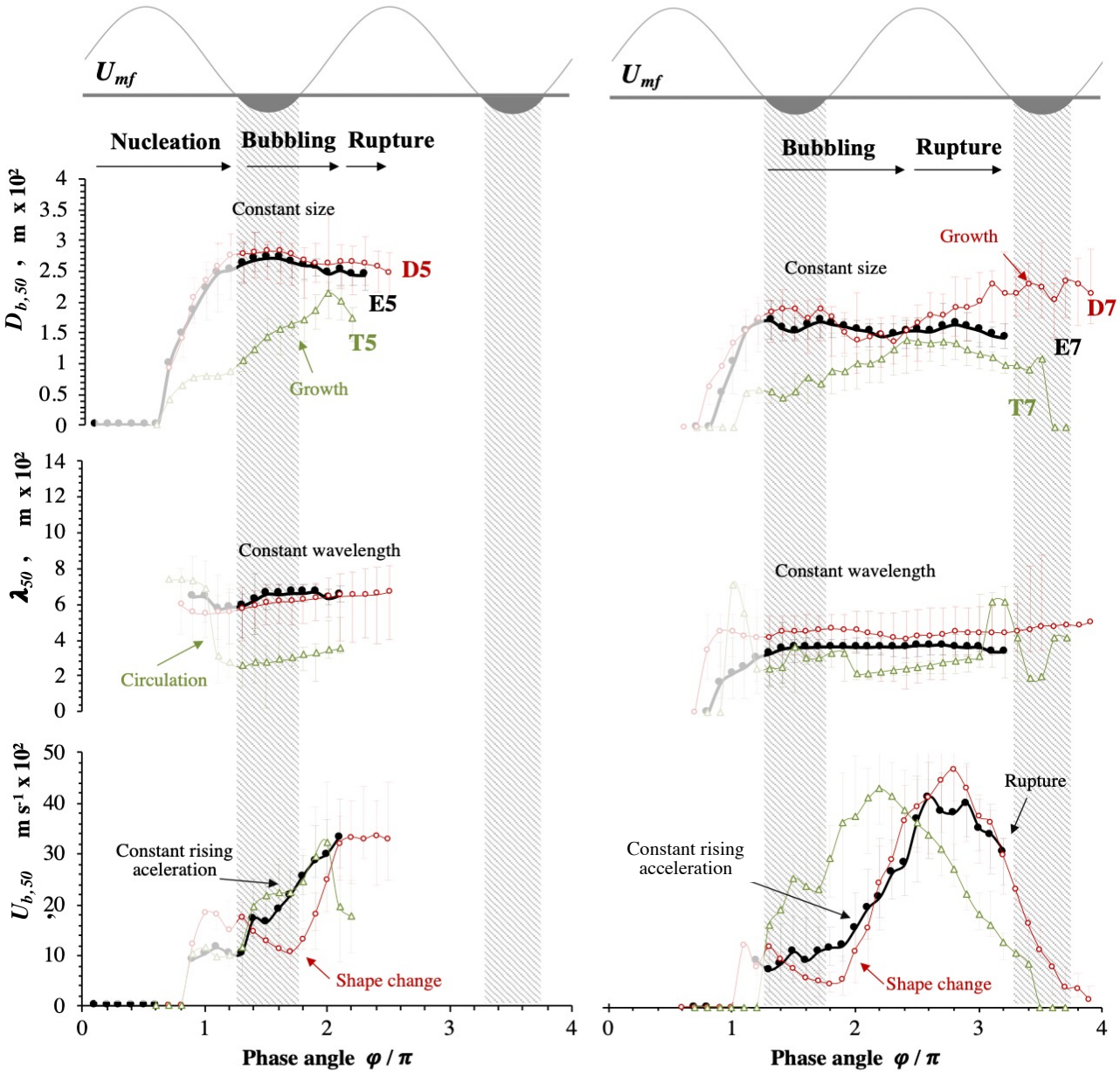

Figure 8- *Prediction of the bubble self-organization in structured beds formed of a single (left, 5 Hz) and a double-row (right, 7 Hz) array of bubbles. Comparison of the experimental (E5, E7) values with the computational (D5/T5, D7/T7) prediction of median bubble size $D_{b,50}$, wavelength λ_{50} and velocity $U_{b,50}$. Error bars denote the range p_{10} to p_{90}.*

immediately acquire their final size, moving upwards under constant acceleration, constant size and constant separation (E5 and E7, Figure 7) until they reach the freeboard, where they decelerate and rupture. As explained earlier, at higher frequency E7, the amount of gas injected in every pulse drops and the duration of the injection shortens, so D_b and λ are reduced in Figure 7. A constant acceleration is observed, even though the bubbles do not grow. This is a distinctive feature of a dynamically structured regime in contradiction with the correlation between bubble size and velocity expected in an emulsion of constant density. In a structured bed, parts of the emulsion transition into a quasi-static regime and each bubble is surrounded by dense areas, where the converging solid flow increases the pressure. The coordinated formation and disintegration of these regions explains why bubbles do not expand. In systems pulsated at higher frequency, E7, we observe two distinct rising accelations, corresponding roughly to the periods where one or two bubbles rows are present in the bed.

Figure 8 shows that TFM models fail to capture the experimentally observed pattern formation. Bubbles grow as they move inwards, reducing the separation during the pulse (T5 and T7 in Figure 8). As a result, bubble size and

separation assume not only much smaller values, but also much broader distributions than what is observed experimentally (E5 and E7). On the contrary, discrete models can track this phenomenon and predict the average properties reasonably well (Table 6). Figure 8 shows that they can also track the key features of the self-organization: (1) the nucleation occurs at the same time when u drops below u_{mf} and (2) the size and separation of the bubbles remain constant throughout the bubbling stage. Nonetheless, they present significant quantitative differences, particularly for the case at 7 Hz involving two rows of bubbles, which suggests that the force balance leading to a stable pattern is not entirely captured by the model. D5 is able to replicate accurately the bubble alternation, and not only the average but the actual bubble size distribution, Figure 9a, and even the wavelength distribution, Figure 9d, as observed in experiments (E5). However, D5 shows a slightly overpredicted mean bubble size and a different bubble shape (Figure 8). This error is not enough to destabilize a small-scale pattern, but it becomes much more significant in the upper part of a taller, two-row lattice, comparing E7 and D7. At the higher frequency of 7 Hz, the prediction (D7) of the nucleation process starts with a more significant error in the separation and when the bubbles approach the freeboard, they are allowed to grow. D7 is still able to provide reasonable average values for D_b and λ but, as reported in Figure 9b and Figure 9e, the simulations do not capture the variability, leading to much broader distributions. Although the nucleation sites alternate for D7, the patterns are more noisy, as reflected in the density maps for D7 in Figure 6. The errors in size and separation are entirely correlated. Inspection of the simulations shows how in every other pulse in D7 a larger bubble appears in the center than on the sides. As it rises, it moves sideways, destabilizing the lattice. It appears that a CFD-DEM framework struggles to represent accurately the stability of a pattern when different bubble rows interact.

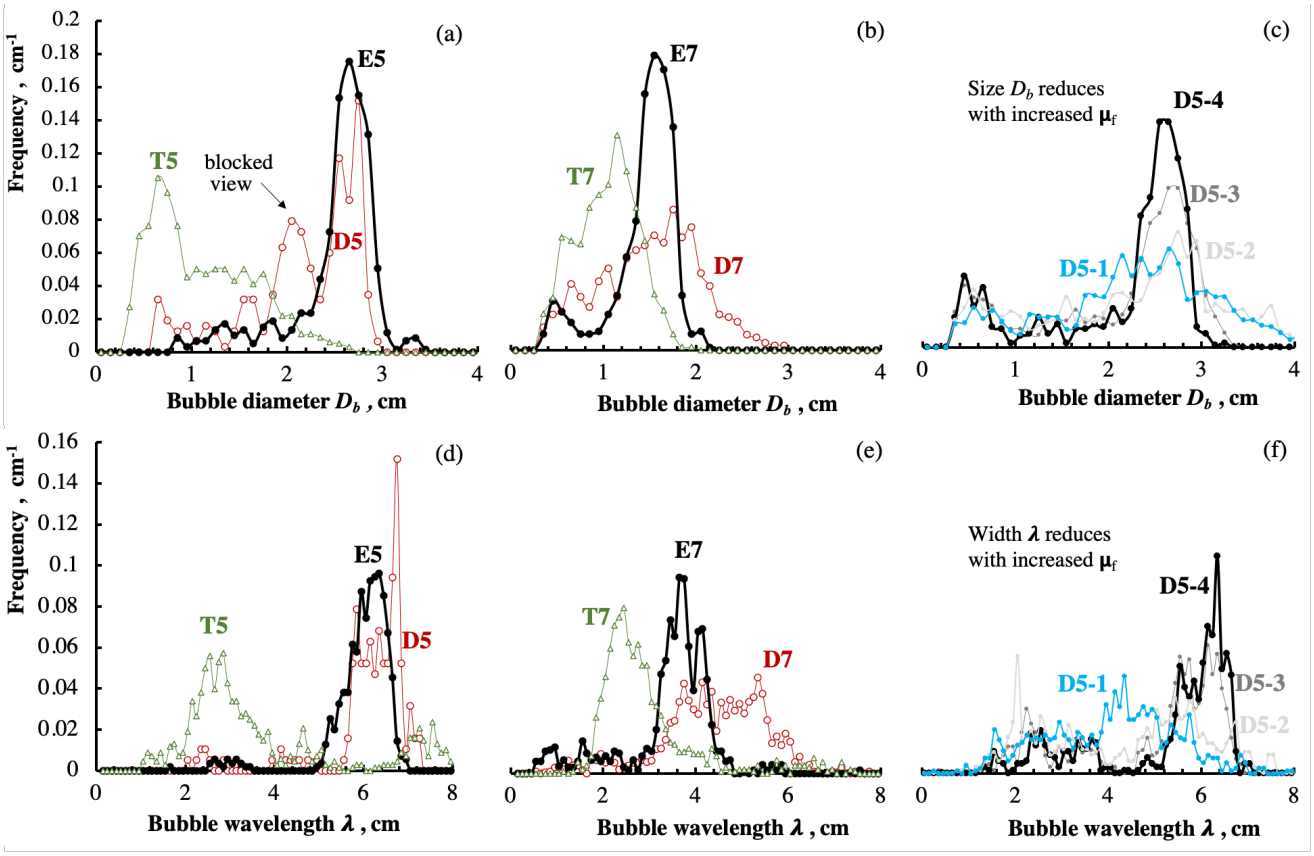

Figure 9 - *Bubble self-organization. Distributions of bubble size D_b and wavelength λ in a structured bed of a single (a & d, 5 Hz) and a double-row array of bubbles (b & e, 7 Hz) and the variation of the predictions through CFD-DEM simulations with decreasing interparticle friction factor, μ_f (c & f). D5-4: $\mu_f = 0.4$; D5-3: $\mu_f = 0.3$; D5-2: $\mu_f = 0.2$: D5-1: $\mu_f = 0.1$.*

Discrete models display also noteworthy trends in the prediction of the bubble rise velocity, U_b, at 5 and 7 Hz. Both are reasonably well predicted (Table 6) but a qualitative difference can be noted in Figure 8. In E5 and E7, bubbles rise at constant acceleration, which is well replicated by hydrodynamic models, T5 and T7, where the bubbles grow as they rise. However, in discrete models, bubbles are compressed when they appear at $\varphi \sim 1.3\pi$, as long as u remains below u_{mf}, i.e., until $\varphi \sim 1.7\pi$. Then, they start to expand and suddenly accelerate and detach from the distributor. This effect is associated with the bubble shape, not the size, but experiments show no such sharp shape changes between the defluidization and fluidization phases in each pulse (videos available as supplementary information). This could partially relate to the effect of polydispersity, whereby experiments using glass beads between 224-250 μm have been simulated as monodisperse, with a size of 238 μm, but it is more likely due to the restrictive dimensions of the domain. The artificially narrow simulation affects the solid packing, which not only introduces an error in the computational u_{mf}, but also makes the solids jam at a lower solid fraction. This can prevent it to disperse at very low gas velocities near the minimum fluidization and instead make the entire bottom section of the bed respond as an elastic network of particle contacts.

The analysis above demonstrates that the drop in bubble size and separation observed in Figure 8 at increasing frequency is not simply the result of reducing the excess gas flow, but a manifestation of complex self-organization behavior correlating the nucleation and motion of a large set of bubbles. It is worth noting that self-assembly in granular media can have different origins, not all related to interparticle friction. Clustering is an example of coherent structures formed due to energy dissipation in inertial systems (Cocco et al., 2010). Many typologies of surface waves in vibrated or pulsed shallow granular layers can be explained in this way, as a purely hydrodynamic effect (Cerda and Tirapegui, 1997; Faraday, 1831). Other ones, however, seem to require energy dissipation through interparticle friction (Francia et al., 2021). At this point, it is unclear whether bubble self-organization responds to a purely local force balance, where the motion of a bubble influences only its immediate neighbors (6 in a triangular lattice) or whether long-range effects are important. However, it is clear that one must operate between spatiotemporally alternating fluidized and fixed bed conditions and under specific parameteric conditions (u_{min}, u_a, f) allowing the interplay between defluidization and fluidization cycles to endow the solid flow with certain memory. Three observations suggest that frictional contacts are key to this effect: (1) bubble nucleation occurs exactly when the bed collapses below u_{mf}, owing to the rearrangement of the powder under very dense conditions; (2) experiments where the gas velocity is always maintained above u_{mf} exhibit no self-organization; (3) any TFM based on hydrodynamic considerations alone and a crude account of the frictional stress fails to capture this phenomenon (Wu et al., 2020).

5.2. Effect of friction on stabilizing the dynamic structure

Figure 6 shows that consecutive pulses become correlated through the effect that existing bubbles have in forming a horizontal channel at $\varphi \sim 0.6\,\pi$. One could argue that, as bubbles rise, they displace the solids in their path into the space between them. Therefore, when the bed collapses, more granular matter is left in between their trajectories, which exerts additional pressure upon the central region of the channel forming at the bottom. This would cause it to flow into the trail of the bubble wake, i.e., in-line nucleation leading to a square lattice. That is a plausible explanation based on hydrodynamic considerations alone and it is in line with TFM predictions, where

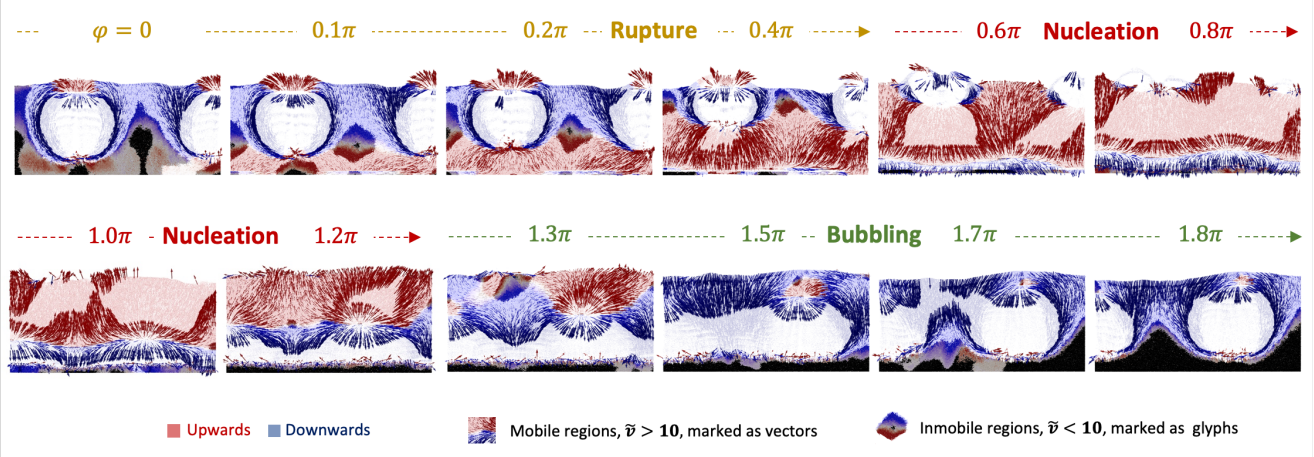

Figure 10- *CFD-DEM simulations at 5 Hz (μ_f =0.35, D5), showing the local solid velocity* $\boldsymbol{v}$ *maps and the granular pivots (areas of low velocity). The areas of low velocity are marked as particles (i.e., spherical glyphs) with solid black for* $\tilde{\boldsymbol{v}} = \boldsymbol{v}/\boldsymbol{d_p} < \mathbf{1}$ *and solid colors for* $\mathbf{1} < \tilde{\boldsymbol{v}} < \mathbf{10}$*. Areas of high velocity are indicated by vectors in red and blue color (*$\mathbf{10} < \tilde{\boldsymbol{v}} < \mathbf{100}$*) or white (*$\tilde{\boldsymbol{v}} > \mathbf{100}$*, 4 × scaled down). The color indicates the direction of the axial velocity,* $\boldsymbol{v_z}$ *(blue for* $\boldsymbol{v_z} < \mathbf{0}$ *and red for* $\boldsymbol{v_z} > \mathbf{0}$*).*

central bubbles cause a long-range circulation and an area of low void fraction in their trail. The reality, however, differs: the channel breaks into the space between the bubbles, not their trails. Previous work (Wu et al., 2017) identified the presence of a downwards compressive solid stress upon the distributor, but it remained unclear what relation it had with the pulsation cycle.

Figure 10 identifies the formation of dense areas in a dynamically structured bed, highlighted as areas of lowest flow velocity. During every oscillation, the bed consolidates when the gas velocity drops below u_{mf} (1.3π - 1.7π). As it collapses, the solids pushed aside by adjacent bubbles create an immobile pyramidal structure (see φ = 1.8π in Figure 10). When the gas velocity rises again (φ = 0), the top of the bed is still collapsing around the gas bubbles that were formed in the previous pulse and that start rising. The drag on the bottom particle cluster increases and the solids are accelerated upwards diagonally and towards the wake of both bubbles, creating two converging points, one in the wake shaped into a pyramid pressed against the distributor, another as a rhomboid at the central tip, where the collapsing and fluidized sections of the bed meet (see φ = 0.1π in Figure 10). When bubbles reach the freeboard, a horizontal channel starts to form at the bottom. The compressive downward stress created in the wake prevents the channel from growing into the path of the existing bubbles; instead, it expands in between them. In the following pulse, a new set of bubbles appears on the trail of the central pivots, creating an alternating set of wake pivots. In this way, central pivots stabilize the current bubbling stage (in a larger system, this is likely to include pivots above and below formed during the preceding and following pulses), while the wake pivots determine the locations of the nucleation points for the following bubbling stage. This synchronization eventually correlates the behavior of three consecutive pulses. In the regions marked with solid colors in Figure 10, the solids are far less mobile and are densely packed. They restrict the circulation and prevent bubbles from moving laterally, suppressing coalescence and leading to narrower velocity distributions. One expects interparticle friction to condition the propensity of the solids to jam in these areas. Furthermore, the range at which the circulation around a single bubble can influence a neighbor must depend on their size and evolution. The dynamics and the stability of the pivots requires further analysis in a larger simulation domain to observe the interaction of a larger number of bubbles, but the direction of the shear planes shown in Figure 10 (the slopes of the pyramid and rhomboids) clearly depends on the frictional nature of the powder.

Figures 11 and 12 visualize how friction affects the stability of self-organization, by showing bubble phase density maps for increasing interparticle friction coefficient μ_f. When using frictionless particles (D5-1), no clear pattern is generated: no energy dissipates through friction and the bed expands unnaturally. As μ_f increases from 0.2 to 0.4 (D5-2 to D5-4), the nucleation becomes reproducible. If $\mu_f \leq 0.2$ (D5-1 and D5-2), the breakage of the horizontal channel renders bubbles of different size. The nucleation sites alternate every pulse, but with high variability (see highlighted positions 1 and 2 in D5-1, Figure 12). As a result, bubbles rise at a different velocity, allowing them to move and grow, and the bubble phase density maps show no clear preferential trajectory (see

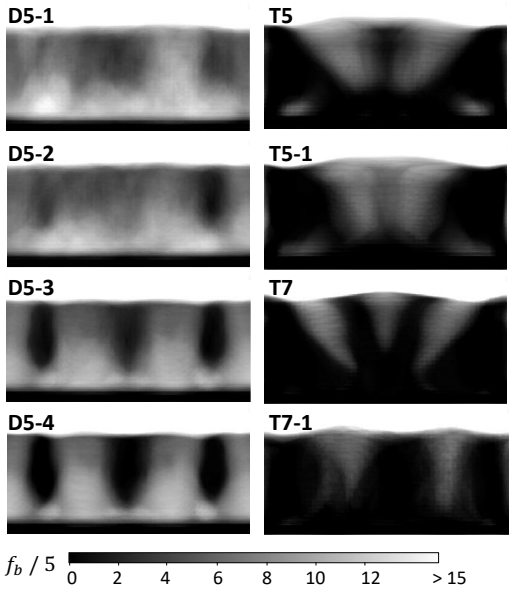

Figure 11 - *Effect of interparticle friction on the bubble phase distribution. Bubble probability density maps, f_b, for varying friction, represented by the interparticle friction coefficient μ_f for discrete simulations (D5-1 to D5-4 varying from μ_f=0.1 to μ_f=0.4) or the frictional packing limit ϕ_f for continuum simulations (T5/T5-1, T7,T7-1). Values in Table 4.*

D5-1 and D5-2 in Figure 11). Since bubbles do not align, they create an asymmetrical compressive stress profile upon the horizontal channel, perpetuating the instability. When energy dissipation increases (D5-3), the nucleation sites start to alternate, forming preferential paths with certain variability (four paths in Figures 11). Dense regions form in the wake, and a periodic compressive stress appears on the distributor with a maximum during every other defluidization cycle, see Figure 12.

Increasing the value of μ_f stabilizes this phenomenon and the interphase boundaries become more reproducible. In other words, friction is not only needed to create the pattern, but it also stabilizes the pattern through the formation of wider dense region s. As μ_f increases, the difference in the axial pressure gradient between pulses becomes more pronounced, forcing the channel-like void to flow into the space between existing bubbles. Figure 12b shows that the pressure gradient reaches its peak around $\varphi = 0.5\pi$, before the channel breaks at $\varphi = 0.7\pi$. In the better structured cases, D5-3 and D5-4, the maximum axial pressure gradient in the nucleation site in consecutive pulses (*A* and *B*) differs by a factor of 3.

The stability of the bubble pattern has a clear effect on the lateral dispersion of the solids. Figure 13 displays time-averaged lateral solid velocity profiles near the bottom of the bed (y = 0.5 cm). In a structured bed, the zero locus points in Figure 13 show areas of converging lateral flow, which, as described in Figure 10, appear in the trail of the bubbles marking the nucleation sites. There are three types of profiles, according to whether a bubble pattern is stabilized or not (videos available as supplementary information). Figure 13d shows how the structured beds,

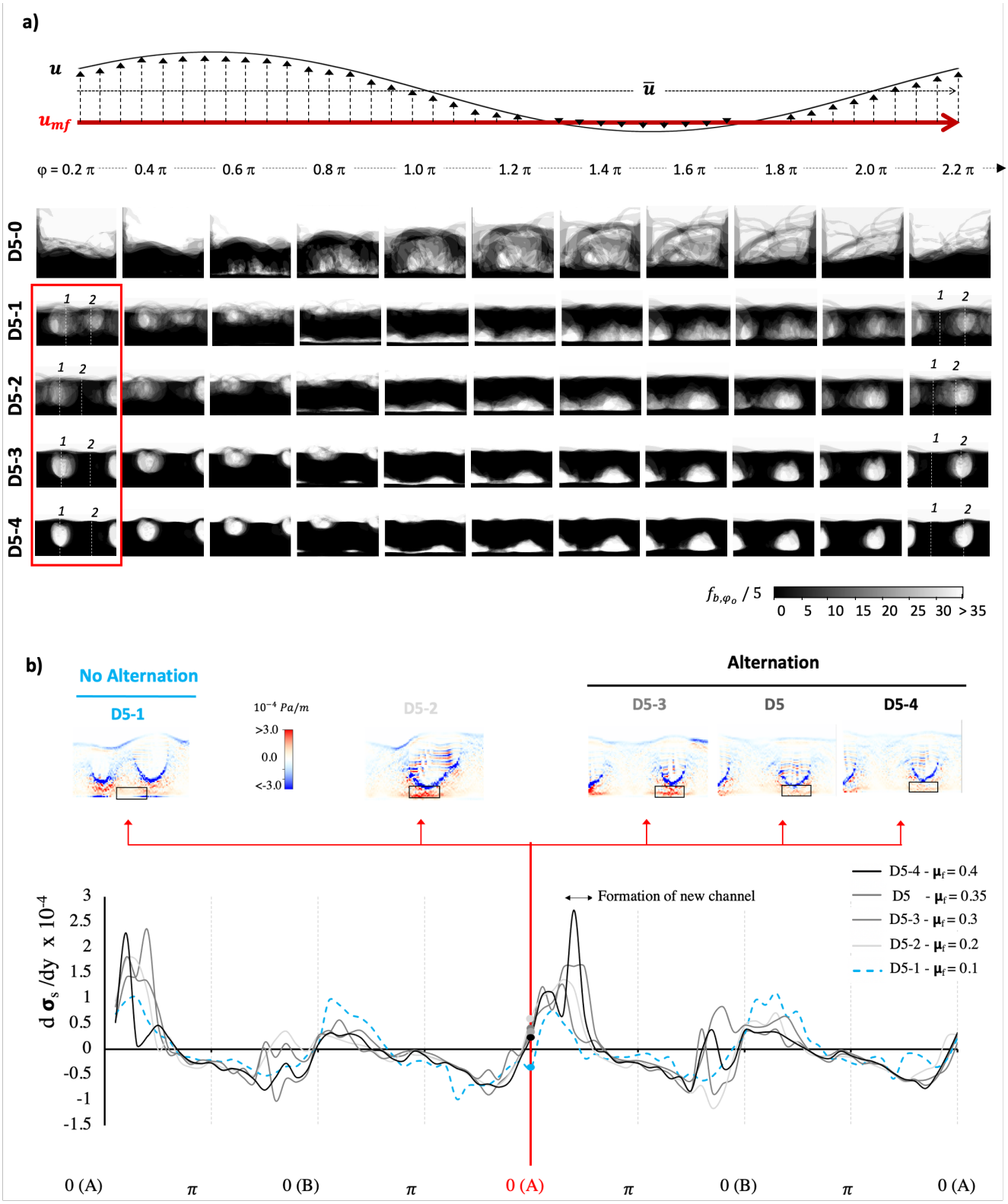

Figure 12. *Effect of interparticle friction on the stability of a dynamically structured fluidized bed. a) Bubble phase probability density maps f_{b,φ_0} for even pulses (i.e., set A) as a function of the friction coefficient μ_f for a single bubble row. b) Time evolution of the axial solid pressure gradient in a bubble nucleation site, for different values of the interparticle friction coefficient μ_f. Sampling region: 0 < y < 1 cm, 3.75 < x < 6.25 cm for D5-1 and D5-2; 0 < y < 1 cm, 5.5 < x < 8 cm for D5, D5-3 and D5-4. The detail shows the memory effect in the contour maps for the solid pressure gradient during the beginning of a new pulse, $\varphi = 0$, highlighted in red in (a), leading to alternation of the nucleation sites (1 and 2) only for a sufficiently high μ_f.*

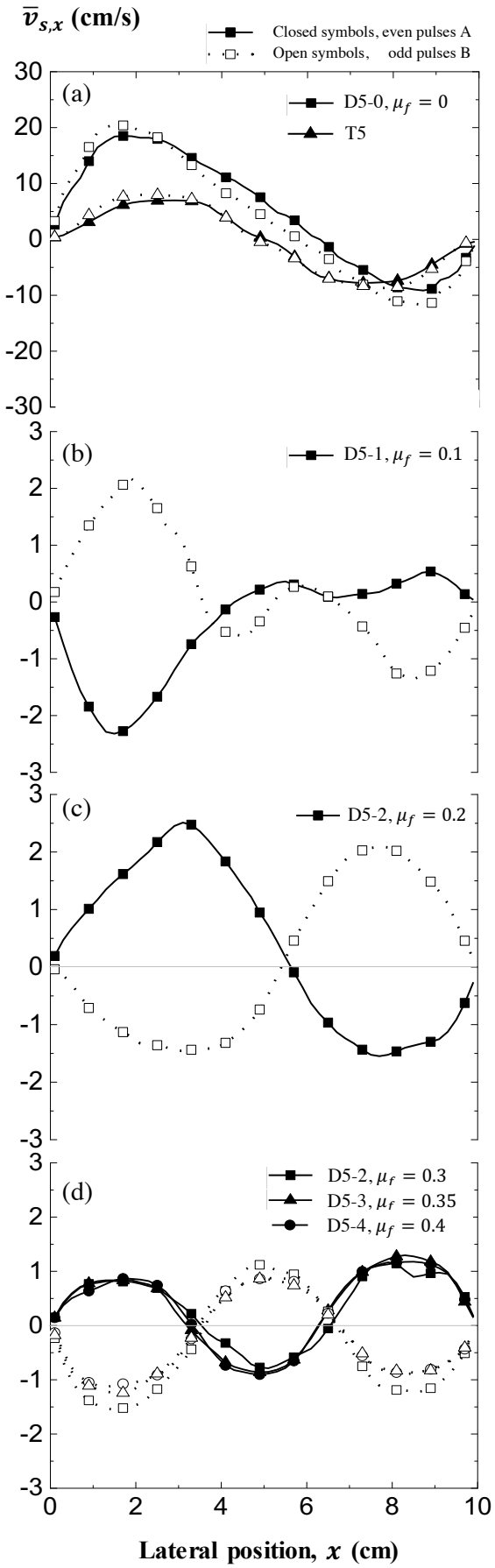

Figure 13. *Time-averaged lateral solid velocity $\bar{v}_{s,x}$ profiles at $\varphi = 0$ near the bottom distributor (y = 0.5 cm) in sets of consecutive pulses, even (A) and odd (B). Effect of interparticle friction coefficient μ_f causing a transition from long-range central recirculation at low energy dissipation (a), to unstructured and central bubble alternation for $\mu_f \leq 0.2$ (b & c) and structured bubbling for $\mu_f \geq 0.3$ (d). Full conditions and nomenclature in Tables 1, 3 & 4.*

$\mu_f \geq 0.3$, display antisymmetric solid velocity profiles in consecutive pulses, forming four zero locus points or nucleation sites (two near the sides and two in the bed) that alternate every pulse. When interparticle friction decreases, the wavelength of the bubble pattern rises beyond the dimensions of the computational domain; thus, for $\mu_f = 0.2$ (D5-2 in Figure 13c), there are only three zero locus points as the result of nucleation sites alternating from a single larger bubble forming in the center to two smaller bubbles forming near the sides. Such a rearrangement is similar to what other researchers have denoted a 1-2 pattern (Bakshi et al., 2018b). However, it must be pointed out that this stems from the impossibility to accommodate the required pattern wavelength in the computational domain, and so it is questionable whether it is a consequence of genuine, scale-independent bubble self-organization or resulting from interactions with the walls. Reducing μ_f further to 0.1 (D5-1) leads to weakly or uncorrelated velocity profiles in Figure 13b. A system with no energy dissipation through friction and classic TFM implementations lead to similar average lateral flows, characterized by a central long-range circulation, already discussed in Figure 4. The dense regions shown in Figure 10, and the lateral velocity profiles shown in figure 13d suggests that the coordinated motion of the bubbles in a structured bed has important implications in the solid flow, compartmentalizing the domain laterally into a series of identical units. In each, the motion and mixing of the solid phase is directly associated with the size and separation of the neighbouring bubbles, and, therefore, one can envisage that they could be externaly controlled through changes to the pulse characteristics.

Figure 14 shows the effect of the interparticle friction coefficient on the evolution of the key median bubble properties during the pulsation. This figure should be compared with Figures 9c and 9f that show the effect on the full distributions of bubble size D_b and wavelength λ. The energy required to mix the emulsion and create the bubble phase increases for increasing μ_f because more kinetic energy is dissipated through friction. Maintaining a constant energy input through drag means that the resulting bubble size reduces significantly by increasing μ_f from 0.1 (D5-1) to 0.4 (D5-4). In a dynamically structured state, there is a strong correlation between the bubble size, D_b, and the pattern wavelength, λ; therefore, a smaller bubble size is in principle expected to lead to a reduced λ, as was shown in Figure 7. However, when μ_f changes, the slope of the dense regions shown in Figure 10 changes too, and hereby, the underlying correlation between a stable pair of D_b and λ. The structure itself breaks down at low values, but as μ_f increases, it becomes more stable and the evolution of D_b and λ approaches the experimental profiles. Only at sufficiently high energy dissipation ($\mu_f \geq 0.3$), a pattern with characteristic narrow size and wavelength distributions emerges, see Figure 9c and 9f. The deviations in the velocity profiles, Figure 14, associated to the changes in the shape of the bubbles during the collapse and fluidization cycles remain unaffected, which is consistent with the hypothesis that they may be the consequence of a narrow simulation domain.

Figure 14 demonstrates that energy dissipation through friction is a fundamental aspect of why a discrete model is able to replicate the phenomenon of dynamic structuring. The pattern itself depends on the formation of intermittent dense areas that restrict the solid circulation and the area of influence of each bubble thereafter depends on the transmission of momentum through long force chains. Friction affects both. It modifies the scale of the dense regions and the direction of the shear planes in Figure 10. As μ_f and energy dissipation increase, the dense regions expand, widening the area of influence of a single bubble, and, therefore, smaller bubbles are stabilized in a wider lattice, as for D5-4. Reducing energy dissipation increases the bubble size and makes dense

regions smaller and less consolidated. The larger bubbles and wider pattern can no longer be accommodated in the computational domain and the pattern breaks down, as for D5-2. TFM models with the current limitations in the constitutive models for the rheology replicate none of these phenomena (Wu et al., 2020).

In a frictionless granular flow, both TFM and CFD-DEM display the same qualitative behavior, whereby the flow recurs with frequency f, with a large central recirculation loop. The variation of the critical packing limit ϕ_f in the TFM framework from T5 to T5-1 and T7 to T7-1 introduces a relatively minor effect to the dynamics. It affects the coalescence of bubbles as they circulate inwards, but it does not have sufficient impact to suppress the circulation of solids in the wake. For TFM to be predictive in these situations, implementations are needed that allow to restrict the solids mobility at high concentration in a realistic way, which is an important theoretical

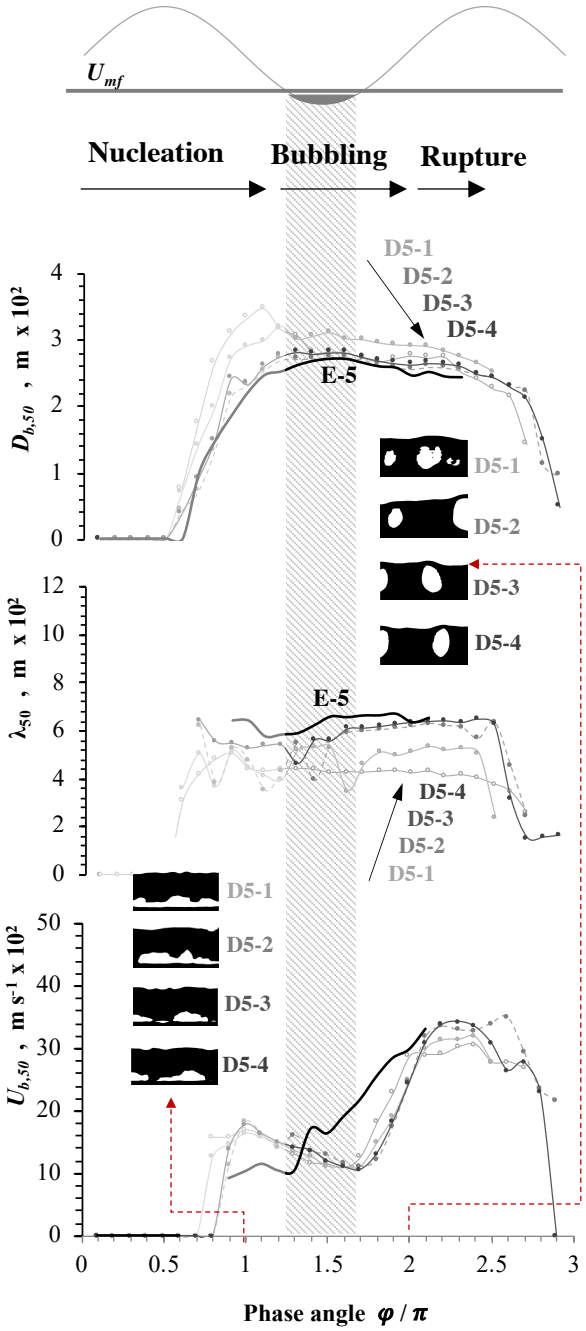

Figure 14. *Effect of increasing the interparticle friction in CFD-DEM simulations from D5-1 (μ_f = 0.1) to D5-4 (μ_f = 0.4), compared with experiments (E5), all at 5 Hz gas pulsing frequency, on the predicted time median bubble size, D_b, wavelength, λ, and velocity, U_b, in the single-row bubble array.*

challenge. In classical frameworks, the friction coefficient plays an overly simplistic role in determining the frictional packing limit ϕ_f. This has a very significant effect on the overall bubbling dynamics by modifying the jamming point, but it is insufficient to predict the emergent spatiotemporal structures formed in the vicinity of minimum fluidization. In essence, the critical state based stress closures for dense granular flows fail to describe the collapsing phase of the pulse and, with it, the dynamic self-organization. Over the last decade, a substantial effort has been devoted to capture dense regimes and extend existing KTGF formulations to account for frictional contact and energy dissipation. In recent work (Wu et al., 2020), we have discussed in detail our perspective on potential improvements of Eulerian-Eulerian models in modelling dynamic bubbling fluidization. Advanced formulations address the problem of a proper description of frictional stress with varying level of detail. These vary from a simple introduction of an effective restitution factor for the *inertial* regime (Jenkins and Berzi, 2010), to a more comprehenshive coupling of existing KTGF formulations with local rheology models for a *transitional* regime, where various formulations exist to blend a $\mu - I$ rheology (Jop et al., 2006) with a yield stress at maximum packing (Chialvo, S., Sundaresan, S. 2013), and, eventually, more complex platforms that introduce non-local correlations depicting microstructural effects in the *quasi-static* regime with additional transport equations (Kamrin and Koval, 2012). Most of them are still in an early developing stage, but they are promising ways forward to tackle a transitional dynamic system, such as the one discussed here.

6. Conclusions

A recent article describes a new class of gas-solid operation, called *dynamically structured fluidized bed*, that borrows characteristics from both fluidized and fixed beds units, by using the right periodic perturbation to make bubbling fully predictable (Francia et al., 2021). The "right" perturbation and the resulting structure, however, depend on particle properties, and are hard to predict computationally. In order to learn how the frictional nature of a powder affects the phenomenon and how models capture the changes in the energy dissipation, this work has analyzed in detail the organization of bubbles in an oscillating bed under varying interparticle friction.

A characteristic evolution of bubble size, separation and velocity is observed, during the nucleation, bubbling and rupture stages of a dynamically structured fluidized bed with single and double-row arrays of bubbles. The self-organization is found to be a manifestation of the energy dissipation. It requires the bed to oscillate around the minimum fluidization (although the average flowrate can be well above it), so that areas can transition locally to a quasi-static flow during the defluidization cycle. Bubbles nucleate at the point when the bed collapses below the minimum fluidization and a gas channel formed at the bottom breaks. As bubbles rise, large dense regions appear in between them and in their wake, transmitting a compressive stress onto the bottom that conditions the formation of the following gas channel endowing the flow with a certain memory. These intermittent solid-like regions form and break every pulse between bubbles and in their wake. They stabilize the bed and restrict the lateral mobility of the solids, preventing long-range solid circulation and helping to compartmentalize the flow. This phenomenon relies on a sufficient level of energy dissipation. In a bed of glass beads, CFD-DEM simulations show that reducing the interparticle friction coefficient beyond 0.2 breaks down the organization. Solids become too mobile, traverse the bubbles wakes and, as a result, the nucleation is no longer synchronized with the formation of dense regions. Classic TFM approaches are not well suited to predict this phenomenon, due to their difficulties in describing a rapid change in the granular rheology near the quasi-static regime. CFD-DEM models do

reproduce the correct level of energy dissipation and replicate the formation of a lattice at different scales and frequencies. However, we have shown that while small-scale CFD-DEM simulations capture the median bubble properties and their evolution through the pulse, they also show qualitative differences in the way bubbles form and in how their shape responds to changes in velocity. Independently of the pulsation conditions, bubbles form when the velocity falls below u_{mf} and rise at a constant size, separation and acceleration. Discrete models predict accurately size and separation in a single bubble row, but simulations of larger, multi-bubble-row arrays display a far higher variability and bias errors in size and separation that make the predicted structure far less stable than the experimental observations. Deviations may be associated with a narrow computational domain and the associated interaction with front and rear walls, but merit further study in a broader domain.

The creation of a structured flow is related to the way in which solid friction dictates the bubble nucleation and how it restricts the solid motion. The identification of the pivots forming in the wake and around bubbles and how stress is transported between neighboring bubbles must now be considered new areas of interest. Furthermore, it is important to study the effects of the self-organisation of bubbles on the macroscopic solid circulation and the resulting gas-solid contact pattern, residence time and lateral dispersion to understand how mixing is affected in a structured bed, and, hereby, evaluate its potential to control solid mixing, stresses, and heat and mass transfer processes for industrial applications.

Nomenclature

C_d	particle drag coefficient, [–]	u_a	pulse amplitude, [m/s]
D_b	bubble size, [m]	u_{min}	pulse minimum velocity, [m/s]
E	Young's modulus, [Pa]	$\hat{u}$	normalized air superficial velocity [–]
$\mathbf{F}_c$	inter-particle contact force, [N]	$\hat{u}$	normalized pulse minimum velocity [–]
$\mathbf{F}_f$	inter-phase contact force, [N]	$\hat{u}_a$	normalized pulse amplitude u_a /u_{mf} [–]
H_0	static bed loading, [m]	*Greek letter*	
I	moment of inertia, [kg·m^2]	β	drag force coefficient, [kg/(m^3·s)]
P	gas pressure, [Pa]	γ_t	normal damping coefficient, [N/m]
Re	particle Reynolds number, [–]	γ_n	tangential damping coefficient, [N/m]
$\mathbf{T}$	torque, [N·m]	$\boldsymbol{\delta}_n$	normal particle overlapping, [m]
$\mathbf{U}_g$	velocity of gas phase, [m/s]	$\boldsymbol{\delta}_t$	tangential particle overlapping, [m]
$\mathbf{U}_s$	velocity of particle, [m/s]	Θ	granular temperature, [m^2/s^2]
V_c	cell volume, [m^3]	θ_f	angle of repose, [º]
V_i	particle volume, [m^3]	ε	volume fraction of gas phase, [–]
W	bed width, [m]	λ	pattern wavelength, [m]
d_s	particle size, [m]	μ_g	viscosity of gas phase, [m/s]
e	restitution coefficient, [–]	μ_f	inter-particle frictional coefficient, [–]
f_b	bubble phase spatial probability [m^{-2}]	μ_w	particle-wall frictional coefficient, [–]
$f_{b\varphi_o}$	bubble phase spatial probability at phase angle φ_o [m^{-2}]	ν	Poisson ratio, [–]

f	frequency of oscillating flow, [Hz]	ζ_i	interpolation coefficient, [–]
$\mathbf{g}$	gravitational acceleration, [9.81 m^2/s]	ρ_g	gas density, [kg/m^3]
k_t	tangential spring coefficient, [N/m]	ρ_s	solids density, [kg/m^3]
k_n	normal spring coefficient, [N/m]	ϕ	volume fraction of solid phase, [–]
t	flow time, [s]	φ	phase angle of the pulse, [–]
u_{mf}	minimum fluidization velocity, [m/s]	$\boldsymbol{\sigma_s}$	solid phase stress tensor
u	superficial gas velocity, [m/s]	$\boldsymbol{\omega}_s$	rotational velocity of particle, [rad/s]

Acknowledgements

The research leading to these results has received funding from an EPSRC "Frontier Engineering" Award (EP/K038656/1, EP/S03305X/1) and an EPSRC Doctoral Training Award (1528604).

References

Akhavan, A., van Ommen, J.R., Nijenhuis, J., Wang, X.S., Coppens, M.-O., Rhodes, M.J., 2008. Improved drying in a pulsation-assisted fluidized bed. Ind. Eng. Chem. Res. 48, 302-309.

Aranson, I.S., Tsimring, L.S., 2009. Granular Patterns. Oxford University Press, Oxford.

Bakshi, A., Altantzis, C., Bershanska, A., Stark, A.K., Ghoniem, A.F., 2018a. On the limitations of 2D CFD for thin-rectangular fluidized bed simulations. Powder Technol. 332, 114-119.

Bakshi, A., Shahnam, M., Gel, A., Li, T., Altantzis, C., Rogers, W., Ghoniem, A.F., 2018b. Comprehensive multivariate sensitivity analysis of CFD-DEM simulations: Critical model parameters and their impact on fluidization hydrodynamics. Powder Technol. 338, 519-537.

Bizon, C., Shattuck, M.D., Swift, J.B., McCormick, W.D., Swinney, H.L., 1998. Patterns in 3D vertically oscillated granular layers: simulation and experiment. Phys. Rev. Lett. 80, 57.

Bougie, J., Duckert, K., 2011. Continuum simulations of shocks and patterns in vertically oscillated granular layers. Phys. Rev. E 83, 011303.

Bougie, J., Moon, S.J., Swift, J., Swinney, H.L., 2002. Shocks in vertically oscillated granular layers. Phys. Rev. E 66, 051301.

Campbell, C.S., 1990. Rapid granular flows. Annu. Rev. Fluid Mech. 22, 57-90.

Carrillo, J.A., Poeschel, T., Saluena, C., 2008. Granular hydrodynamics and pattern formation in vertically oscillated granular disk layers. J. Fluid Mech. 597, 119-144.

Cerda, E., Tirapegui, E., 1997. Faraday's Instability for Viscous Fluids. Phys. Rev. Lett. 78, 859-862.

Chialvo, S., Sun, J., Sundaresan, S., 2012. Bridging the rheology of granular flows in three regimes. Phys. Rev. E 85, 021305.

Chialvo, S., Sundaresan, S., 2013. A modified kinetic theory for frictional granular flows in dense and dilute regimes. Phys. Fluids 25, 070603.

Clément, E., Labous, L., 2001. Pattern formation in a vibrated franular layer, in: Pöschel, T., Luding, S. (Eds.), Granular Gases. Springer, Berlin, pp. 233-243.

Clément, E., Vanel, L., Rajchenbach, J., Duran, J., 1996. Pattern formation in a vibrated two-dimensional granular layer. Phys. Rev. E 53, 2972.

Cocco, R., Shaffer, F., Hays, R., Reddy Karri, S.B., Knowlton, T., 2010. Particle clusters in and above fluidized beds. Powder Technol. 203, 3-11.

Coppens, M.-O., Regelink, M.A., van den Bleek, C.M., 2002. Pulsation induced transition from chaos to periodically ordered patterns in fluidised beds, Proc. of 4th World Congr. on Part. Technol. (WCPT), Sydney, pp. 1-8.

Coppens, M.-O., van Ommen, J.R., 2003. Structuring chaotic fluidized beds. Chem. Eng. J. 96, 117-124.

Courant, R., Friedrichs, K., Lewy, H., 1967. On the partial difference equations of mathematical physics. IBM J. 11, 215-234.

de Martín, L., Ottevanger, C., van Ommen, J.R., Coppens, M.-O., 2018. Universal stability curve for pattern formation in pulsed gas-solid fluidized beds of sandlike particles. Phys. Rev. Fluids 3, 034303.

Ding, Z., Tiwari, S.S., Tyagi, M., Nandakumar, K., 2021. Computational fluid dynamic simulations of regular bubble patterns in pulsed fluidized beds using a two-fluid model. The Canadian Journal of Chemical Engineering In press, In press.

Douady, S., Fauve, S., Laroche, C., 1989. Subharmonic instabilities and defects in a granular layer under vertical vibrations. Europhys. Lett. 8, 621.

Faraday, M., 1831. On a peculiar class of acoustical figures; and on certain forms assumed by groups of particles upon vibrating elastic surfaces. Philos. Trans. R. Soc. London 121, 299-340.

Foerster, S.F., Louge, M.Y., Chang, H., Allia, K., 1994. Measurements of the collision properties of small spheres. Phys. Fluids 6, 1108-1115.

Francia, V., Wu, K., Coppens, M.-O., 2021. Dynamically structured fluidization: Oscillating the gas flow and other opportunities to intensify gas-solid fluidized bed operation. Chem. Eng. Process. 159, 108143.

Gidaspow, D., 1994. Multiphase Flow and Fluidization: Continuum and Kinetic Theory Descriptions. Academic press, New York.

Gidaspow, D., Bezburuah, R., Ding, J., 1991. Hydrodynamics of circulating fluidized beds: Kinetic theory approach, Proc. of 7th Eng. Found. Conf. on Fluidization, Brisbane, pp. 75-82.

Goniva, C., Kloss, C., Deen, N.G., Kuipers, J.A.M., Pirker, S., 2012. Influence of rolling friction on single spout fluidized bed simulation. Particuol. 10, 582-591.

Hernández-Jiménez, F., Sánchez-Delgado, S., Gómez-García, A., Acosta-Iborra, A., 2011. Comparison between two-fluid model simulations and particle image analysis & velocimetry (PIV) results for a two-dimensional gas–solid fluidized bed. Chem. Eng. Sci. 66, 3753-3772.

Ireland, E., Pitt, K., Smith, R., 2016. A review of pulsed flow fluidisation; the effects of intermittent gas flow on fluidised gas–solid bed behaviour. Powder Technol. 292, 108-121.

Jackson, R., 2000. The Dynamics of Fluidized Particles. Cambridge University Press, Cambridge.

Jaeger, H.M., Nagel, S.R., 1992. Physics of the granular state. Science 255, 1523-1531.

Jaeger, H.M., Nagel, S.R., Behringer, R.P., 1996. Granular solids, liquids, and gases. Rev. Mod. Phys. 68, 1259.

Jenkins, J.T., Berzi, D., 2010. Dense inclined flows of inelastic spheres: tests of an extension of kinetic theory. Granular Matter 12, 151-158.

Jia, D., Bi, X., Lim, C.J., Sokhansanj, S., Tsutsumi, A., 2016. Biomass drying in a pulsed fluidized bed without inert bed particles. Fuel 186, 270-284.

Jia, D., Bi, X., Lim, C.J., Sokhansanj, S., Tsutsumi, A., 2017. Gas-solid mixing and mass transfer in a tapered fluidized bed of biomass with pulsed gas flow. Powder Technol. 316, 373-387.

Jia, D., Cathary, O., Peng, J., Bi, X., Lim, C.J., Sokhansanj, S., Liu, Y., Wang, R., Tsutsumi, A., 2015. Fluidization and drying of biomass particles in a vibrating fluidized bed with pulsed gas flow. Fuel Process. Technol. 138, 471-482.

Jop, P., Forterre, Y., Pouliquen, O., 2006. A constitutive law for dense granular flows. Nature 441, 727-730.

Kamrin, K., Koval, G., 2012. Nonlocal constitutive relation for steady granular flow. Phys. Rev. Lett. 108, 178301.

Kawaguchi, T., Miyoshi, A., Tanaka, T., Tsuji, Y., 2001. Discrete particle analysis of 2D pulsating fluidized bed, Proc. of 4th Int. Conf. on Multiphase Flow, New Orleans, No. 838.

Kunii, D., Levenspiel, O., 2013. Fluidization Engineering. Butterworth-Heinemann, Boston.

Lun, C., Savage, S.B., Jeffrey, D., Chepurniy, N., 1984. Kinetic theories for granular flow: inelastic particles in Couette flow and slightly inelastic particles in a general flowfield. J. Fluid Mech. 140, 223-256.

Melo, F., Umbanhowar, P.B., Swinney, H.L., 1994. Transition to parametric wave patterns in a vertically oscillated granular layer. Phys. Rev. Lett. 72, 172.

Melo, F., Umbanhowar, P.B., Swinney, H.L., 1995. Hexagons, kinks, and disorder in oscillated granular layers. Phys. Rev. Lett. 75, 3838.

Mikami, T., Kamiya, H., Horio, M., 1998. Numerical simulation of cohesive powder behavior in a fluidized bed. Chem. Eng. Sci. 53, 1927-1940.

Müller, C., Holland, D., Sederman, A., Scott, S., Dennis, J., Gladden, L., 2008. Granular temperature: comparison of magnetic resonance measurements with discrete element model simulations. Powder Technol. 184, 241-253.

Pak, H., Behringer, P., 1994. Bubbling in vertically vibrated granular materials. Nature 371, 231-233.

Pouliquen, O., Forterre, Y., 2002. Friction law for dense granular flows: application to the motion of a mass down a rough inclined plane. J. Fluid Mech. 453, 133-151.

Rüdisüli, M., Schildhauer, T.J., Biollaz, S.M.A., van Ommen, J.R., 2012. Scale-up of bubbling fluidized bed reactors — A review. Powder Technol. 217, 21-38.

Schaeffer, D.G., 1987. Instability in the evolution equations describing incompressible granular flow. J. Differ. Equations 66, 19-50.

Silbert, L.E., Ertas, D., Grest, G.S., Halsey, T.C., Levine, D., Plimpton, S.J., 2001. Granular flow down an inclined plane: Bagnold scaling and rheology. Phys. Rev. E 64, 051302.

Syamlal, M., Rogers, W., O'Brien, T.J., 1993. MFIX documentation: Theory guide. National Energy Technology Laboratory, Department of Energy, Technical Note DOE/METC-95/1013 and NTIS/DE95000031.

Toomey, R., Johnstone, H.F., 1952. Gaseous fluidization of solid particles. Chem. Eng. Progr. 48, 220-226.

Tsimring, L.S., Aranson, I.S., 1997. Localized and cellular patterns in a vibrated granular layer. Phys. Rev. Lett. 79, 213.

van de Klundert, R., 2001. Pattern formation in pulsated fludized beds and vertically vibrated granular layers. Master thesis, Delft University of Technology.

van den Bleek, C.M., Coppens, M.-O., Schouten, J.C., 2002. Application of chaos analysis to multiphase reactors. Chem. Eng. Sci. 57, 4763-4778.

van der Hoef, M., Ye, M., van Sint Annaland, M., Andrews, A., Sundaresan, S., Kuipers, J.A.M., 2006. Multiscale modeling of gas-fluidized beds. Adv. Chem. Eng. 31, 65-149.

van Wachem, B., Schouten, J.C., van den Bleek, C.M., Krishna, R., Sinclair, J., 2001. Comparative analysis of CFD models of dense gas–solid systems. AlChE J. 47, 1035-1051.

Wang, X., Rhodes, M., 2005. Pulsed fluidization—a DEM study of a fascinating phenomenon. Powder Technol. 159, 142-149.

Wu, K., de Martín, L., Coppens, M.-O., 2017. Pattern formation in pulsed gas-solid fluidized beds–the role of granular solid mechanics. Chem. Eng. J. 329, 4-14.

Wu, K., de Martín, L., Mazzei, L., Coppens, M.-O., 2016. Pattern formation in fluidized beds as a tool for model validation: A two-fluid model based study. Powder Technol. 295, 35-42.

Wu, K., Francia, V., Coppens, M.-O., 2020. Dynamic viscoplastic granular flows: A persistent challenge in gas-solid fluidization. Powder Technol. 365, 172-185.

Yang, L., Padding, J.T., Kuipers, J.A.M., 2016a. Modification of kinetic theory of granular flow for frictional spheres, Part I: Two-fluid model derivation and numerical implementation. Chem. Eng. Sci. 152, 767-782.

Yang, L., Padding, J.T., Kuipers, J.A.M., 2016b. Modification of kinetic theory of granular flow for frictional spheres, part II: Model validation. Chem. Eng. Sci. 152, 783-794.